# Ocean bottom distributed acoustic sensing for T-wave detection and seismic ocean thermometry

Zhichao Shen[1] and Wenbo Wu[1]

[1]Woods Hole Oceanographic Institution

September 5, 2023

# Ocean bottom distributed acoustic sensing for oceanic seismicity detection and seismic ocean thermometry

**Zhichao Shen[1] and Wenbo Wu[1]**

[1]Department of Geology and Geophysics, Woods Hole Oceanographic Institution, Woods Hole, MA, USA

Corresponding author: Zhichao Shen (zhichao.shen@whoi.edu)

**Key Points:**

- We develop a curvelet denoising scheme for ocean bottom distributed acoustic sensing to enhance *T*-wave signals.
- The denoised distributed acoustic sensing data detects three times more *T*-wave events than cabled ocean bottom seismometers.
- The improved detection capability makes more small repeating earthquakes usable for seismic ocean thermometry.

## Abstract

A *T*-wave is a seismo-acoustic wave that can travel a long distance in the ocean with little attenuation, making it valuable for monitoring remote tectonic activity and changes in ocean temperature using seismic ocean thermometry (SOT). However, current high-quality *T*-wave stations are sparsely distributed, limiting the detectability of oceanic seismicity and the spatial resolution of global SOT. The use of ocean bottom distributed acoustic sensing (OBDAS), through the conversion of telecommunication cables into dense seismic arrays, is a cost-effective and scalable means to complement existing seismic stations. Here, we systematically investigate the performance of OBDAS for oceanic seismicity detection and SOT using a 4-day Ocean Observatories Initiative community experiment offshore Oregon. We first present *T*-wave observations from distant and regional earthquakes and develop a curvelet denoising scheme to enhance *T*-wave signals on OBDAS. After denoising, we show that OBDAS can detect and locate more and smaller *T*-wave events than regional OBS network. During the 4-day experiment, we detect 92 oceanic earthquakes, most of which are missing from existing catalogs. Leveraging the sensor density and cable directionality, we demonstrate the feasibility of source azimuth estimation for regional Blanco earthquakes. We also evaluate the SOT performance of OBDAS using pseudo-repeating earthquake *T*-waves. Our results show that OBDAS can utilize repeating earthquakes as small as M3.5 for SOT, outperforming ocean bottom seismometers. However, ocean ambient natural and instrumental noise strongly affects the performance of OBDAS for oceanic seismicity detection and SOT, requiring further investigation.



## Plain Language Summary

Oceanic earthquakes can produce loud sounds in the ocean. These sounds usually arrive at a seismic station as the tertiary wave, a so-called *T*-wave, following the arrival of the primary *P*-wave and secondary *S*-wave. *T*-waves can propagate thousands of kilometers in the ocean's SOFAR (SOund Fixing And Ranging) channel with little energy loss. Thus, they are useful for monitoring earthquakes and ocean temperature changes. However, currently available instruments for measuring these waves are limited. Recently, a new type of technique, Distributed Acoustic Sensing (DAS), provides an opportunity to expand the seismic-recording capability in the ocean. Ocean bottom distributed acoustic sensing (OBDAS) can effectively turn submarine telecommunication cables into dense seismic sensors that complement conventional seismometers. In this study, we explore the OBDAS potential for *T*-wave detection. With a 4-day OBDAS community experiment offshore Oregon, we demonstrate that OBDAS does a better job than a conventional seismic network for detecting *T*-waves when a specifically designed denoising scheme is applied. In addition, OBDAS has the potential to measure ocean temperature changes using more repeating earthquakes of smaller magnitudes, outperforming conventional sensors. However, the accuracy of the OBDAS system can be strongly affected by various types of noise, which requires further research.

## 1 Introduction

As a tertiary arrival after the *P*-wave and *S*-wave on seismograms, the seismo-acoustic *T*-wave propagates horizontally at a speed of ~1.5 km/s along the ocean SOund Fixing And Ranging (SOFAR) channel, where ocean sound speed reaches a minimum (Tolstoy & Ewing, 1950; Linehan, 1940). Generated from earthquakes and a number of acoustic sources in the water column, *T*-waves can travel a long distance (>1000 km) with little energy loss. *T*-waves exhibit spindle-shaped, high-frequency (>1 Hz) waveforms on hydrophones (Fox et al, 1995), ocean bottom seismometers (OBS; Hamada, 1985), autonomous MERMAID floats (Simon et al., 2021), and even land stations (e.g., Buehler & Shearer, 2015). Since their early documentations in the 1930s (Jagger, 1930; Collins, 1936), *T*-waves have been widely used to monitor oceanic seismicity (Fox et al., 2001; Smith et al., 2002; Dziak et al, 2004; Hanson & Bowman, 2006; Parnell-Turner et al., 2022) and volcanism (Wech et al, 2018; Tepp & Dziak, 2021), promote tsunami warning (Okal & Talandier, 1986; Matsumoto et al., 2016), determine earthquake properties (Walker et al., 1992; de Groot-Hedlin, 2005), discriminate explosive and seismic sources (Talandier & Okal, 2001, 2016), infer detached slabs (Okal, 2001), and constrain crustal attenuation (Koyanagi et al., 1995; Zhou et al., 2021), significantly broadening our understanding of tectonic process in the remote ocean (Dziak et al., 2012) and seismo-acoustic wave genesis and propagation (Okal, 2008).

*T*-waves can also provide valuable insights to long-term deep ocean temperature changes. With more than 90% of excess heat due to the greenhouse effect being absorbed, the ocean is experiencing a secular warming trend of ~0.02 K per decade (Wunsch, 2016). Since the ocean is an efficient hydroacoustic transmitter and sound speed in seawater increases with temperature, Wu et al. (2021) developed seismic ocean thermometry (SOT) to quantify basin-scale ocean temperature changes from the travel time changes of *T*-waves generated by repeating earthquakes. This idea was inspired by the ocean acoustic tomography proposed by Munk and Wunsch (1979). While the latter concept, which utilizes active sources, has achieved great success (Munk et al., 1994; ATOC Consortium, 1998), the cost-efficient SOT approach has shown great potential to complement modern Argo Climatology data (Riser et al., 2016) in a passive way. Applying SOT to the equatorial Indian Ocean revealed ocean dynamic signals at various time scales and depths including seasonal changes, meso-scale eddies and equatorial waves (Wu et al., 2021; Callies et al., 2023), that demonstrates its potential to complement existing ocean temperature observations.

A further expansion of oceanic seismicity monitoring and SOT to the global ocean requires the establishment of long-term stations to record high-quality *T*-waves. However, suitable *T*-wave stations remain sparsely distributed, the Comprehensive Nuclear-Test-Ban Treaty Organization (CBTBO) operating a handful of hydrophone stations (Figure 1a), and with other networks maintaining a few island stations and a limited number of offshore cabled sites, greatly limiting the spatial coverage of oceanic seismicity monitoring and global SOT. In particular, the coverage of the Arctic and Southern Oceans (Figure 1a) is extremely poor, highlighting an urgent need for more observations to fill the gap. Meanwhile, deploying and maintaining long-term, high-quality

*T*-wave instrumentation in the harsh ocean environment is a significant logistical and financial challenge.

Distributed acoustic sensing (DAS) is a new and promising technology that offers a cost-efficient and scalable solution for deploying large-aperture, long-term, dense seismic arrays. By converting Rayleigh-type backscattering due to intrinsic fiber impurities to longitudinal strain or strain rate, DAS repurposes pre-existing telecommunication fiber-optic cables into arrays of thousands of vibration sensors (Hartog, 2017). With up to ~100 km aperture and sensor spacing of a few meters, DAS can record high frequency wavefields at unprecedented spatiotemporal resolution, making it a compelling tool for a range of geophysical settings (Zhan, 2020; Lindsey & Martin, 2021). In underwater environments, ocean bottom DAS (OBDAS) has been successfully used as a very broadband instrument (Ide et al., 2021) to detect earthquakes (Lior et al., 2021), illuminate seafloor faults (Lindsey et al., 2019), characterize marine sediment (Spica et al., 2020; Cheng et al., 2021; Viens et al., 2022), monitor ocean dynamics (Sladen et al., 2019; Williams et al., 2019, 2022) and map offshore wind turbines (Williams et al., 2021). With air-gun shots, Matsumoto et al., (2021) demonstrated that OBDAS is effective in sensing hydroacoustic signals across a broad frequency range from a tenth to a few tens of Hz. Recently, Ugalde et al., (2022) presented *T*-wave observations on OBDAS in the Canary Islands from several regional and distant earthquakes. However, due to limited observations, the performance of OBDAS for oceanic seismicity detection and SOT has not yet been systematically investigated.

In this study, we use data from a 4-day community experiment conducted offshore central Oregon to examine *T*-waves on OBDAS. To identify potential *T*-wave candidates on OBDAS, we first build a *T*-wave catalog using Ocean Networks Canada cabled OBS and hydrophone array. With this catalog, we identify *T*-wave observations on OBDAS and develop a curvelet denoising algorithm to enhance *T*-wave signal-to-noise ratios. The application of curvelet denoising on OBDAS enables us to detect 92 *T*-wave events, three times the number identified in the NEPTUNE *T*-wave catalog. Meanwhile, the OBDAS cable directionality enables us to constrain the source azimuth of regional Blanco earthquakes through array beamforming. With the enhanced detection capability, we propose a new workflow for SOT with OBDAS by taking advantage of a larger number of usable small repeating earthquakes compared to the OBS data. Lastly, we also discuss the noise in OBDAS data, which requires further investigation.

## 2 Data

The Ocean Observatory Initiative (OOI) Regional Cable Array (RCA) offshore central Oregon is a long-term infrastructure designed to facilitate integrated investigations into both volcanic and coastal systems (Kelly et al., 2014). It provides real-time telemetry for over 140 instruments, including OBSs, remote access fluid samplers, DNA samplers, acoustic doppler current profilers and so on. The OOI RCA observatory is powered by and communicates through two telecommunication fiber-optic subsea backbone cables, with the northern branch extending to

Axial Seamount and the southern branch running to the Oregon shelf (Figure 1b). Since 2015, five OBSs have been deployed near Southern hydrate ridge (Figure 1b) in order to monitor oceanic seismicity, track melt migration, and whale vocalizations, with four located at the ridge summit at a water depth of ~800 m (HYS11-14) and one situated at the slope base at a water depth of ~2900 m (HYSB1).

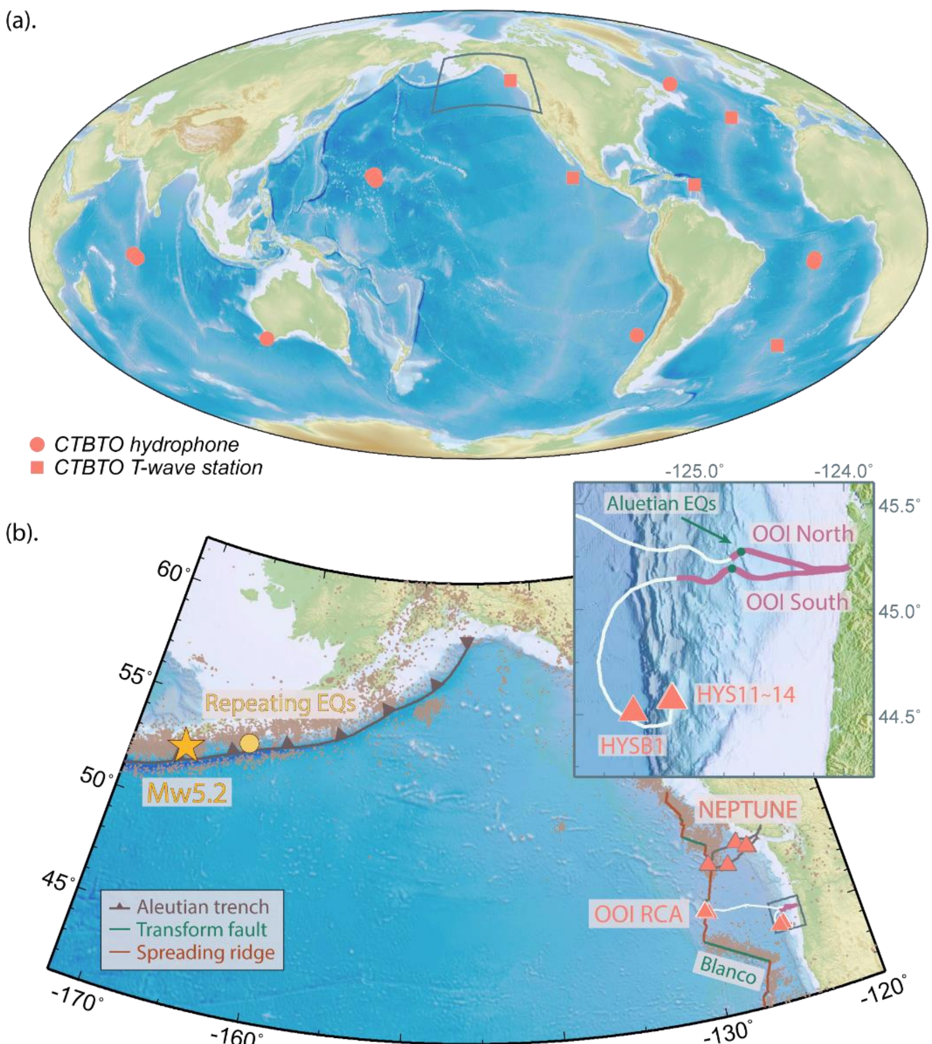


**Figure 1**. The CTBTO hydrophone network and our study region. (a). Global CTBTO hydrophones and *T*-wave stations. The gray box illustrates our study region. (b). Map view of our study region with background tectonics and seismicity, cabled ocean observatories (ONC NEPTUNE and OOI RCA; orange triangles), and OOI OBDAS. The insert panel (top right) is a zoom-in view of OBDAS (purple lines) and OBSs at OOI. The green dots indicate the locations where the OOI North and South cables turn southward. White lines denote entire backbone cables. The green arrow represents the *T*-wave propagation direction from Aleutian earthquakes.

During a scheduled maintenance period of the OOI RCA platform in November 2021, a four-day community experiment was conducted to explore the potential of submarine DAS for observing seismic, oceanographic, acoustic, and geodetic processes (Wilcock et al., 2023). Specifically, between November 1st and 5th, two fiber-optic backbone cables were temporarily converted to OBDAS arrays, referred to as OOI North and OOI South. The OOI North array had two optical fibers connected to Optasense QuantX and Silixa iDASv3 interrogators, respectively, to record OBDAS data up to the first optical repeater located at ~65 km from the shore, with a gauge length of 30 m during most of the experiment. OOI South had one fiber for collecting OBDAS data using another Optasense QuantX interrogator, while the other fiber was used for distributed temperature sensing. The first optical repeater of OOI South is located ~95 km away, and the gauge length is set at 50 m. With a channel spacing of ~2 m, the OOI North array has a total number of 32,600 channels whereas the OOI South array consists of 47,500 channels. During the experiment, both arrays recorded abundant low-frequency acoustic signals such as whale calls and ship noise (Wilcock et al, 2023). In this study, we solely focus on the Optasense OBDAS data since the data from both arrays are available, allowing for a direct and straightforward comparison.

Located ~400 km northeast of the RCA network, the Ocean Networks Canada (ONC) North-East Pacific Undersea Networked Experiments (NEPTUNE) off the coast of British Columbia is another multidisciplinary observatory that has been used to monitor the earth/ocean system since 2009. The NEPTUNE network consists of more than 14 ocean bottom seismometers, accelerometers and hydrophones that are mainly distributed across four sites: Clayoquot Slope, Endeavour Ridge, Cascadia Basin, and Barkley Canyon (Barnes et al., 2008; Figure 1b). Both the OOI and NEPTUNE networks have high sensitivity to *T*-waves from earthquakes at mid-ocean ridges and transform faults in the northeast Pacific and the Aleutian subduction zone (Dziak et al., 2012; Tréhu et al., 2018).

## 3 Regional *T*-wave event catalog using NEPTUNE

During the four-day community DAS experiment, the global ISC (International Seismological Centre; Bondár & Storchak, 2011) catalog only documents a few earthquakes in the northeast Pacific that might produce high-quality *T*-waves (Table S1). To search for a more complete set of *T*-wave events, we download vertical component seismograms from eight NEPTUNE stations, with two at each site (Figure 2a), remove their instrument responses, mean values and linear trends, and band-pass filter the data between 4 and 6 Hz, which is favorable for high-quality *T*-wave observations (Okal, 2008). We implement a recursive short-time-average/long-time-average (STA/LTA) algorithm (Withers et al., 1998) to detect *T*-waves on each individual station. With a STA of 5 s and LTA of 50 s, potential *T*-waves are identified once their STA/LTA ratios exceed a threshold of 1.8, which corresponds to ~12 times the median absolute deviation of daily STA/LTA. We then clean all the picks in a 50-s sliding window and only retain detections if *T*-waves are observed at more than three sites (Figure 2c). After careful visual examinations, we establish a total of 27 *T*-wave events (Table S1). Our NEPTUNE catalog includes six earthquakes in the ISC catalog with three M4.0+ events in the Aleutian trench, two small ones north of NEPTUNE and a

Mw4.4 event near the coast of Northern California (Figure 2; Table S1), confirming the robustness of our method.

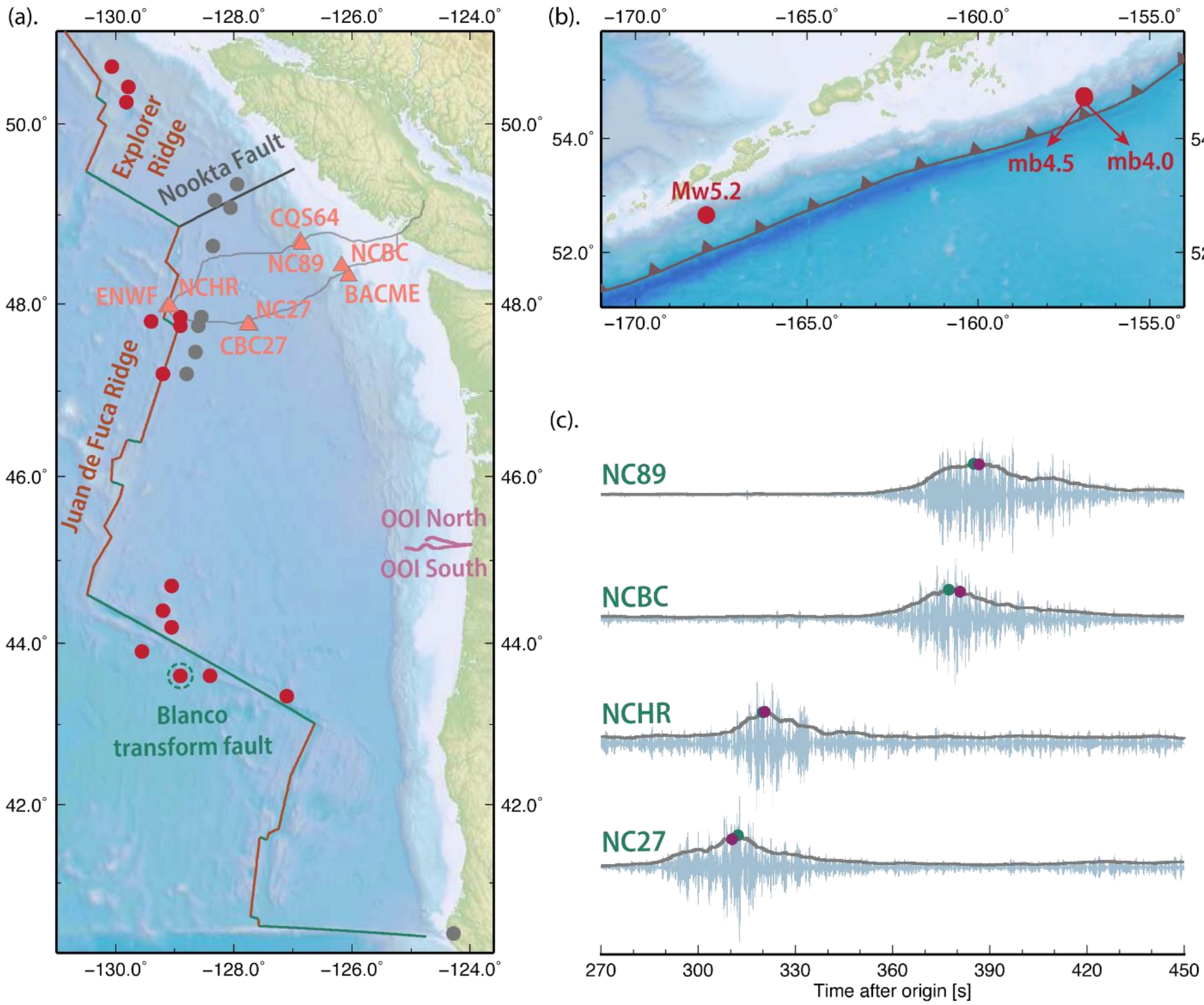


**Figure 2**. Ocean Networks Canada NEPTUNE *T*-wave catalog. (a). Regional seismicity detected using *T*-waves at the NEPTUNE networks. The red and gray circles indicate earthquakes with detectable and undetectable *T*-waves on OOI OBDAS, respectively. The green dashed circle denotes the event shown in (c). (b). Similar to (a) but for earthquakes along the Aleutian trench. (c). *T*-waves detected on the NEPTUNE array from a Blanco earthquake. The gray lines indicate *T*-wave envelopes smoothed by a 5-s sliding window. The green and purple solid circles represent the picked and predicted *T*-wave arrivals (envelope peaks), respectively.

We find four non-ISC events that generate clear *P*-waves and *S*-waves at nearby onshore stations (Figure S1). To determine their origin times and locations, we perform a grid search with an interval of 0.02°, minimizing the L1 norm of the time differences between predicted and manually picked P and S arrivals (see supplementary text S1 for more details; Kennett & Engdahl, 1991). All of them are located in regions of active background seismicity close to the continental shelf –

two near the Explorer Ridge and the other two to the north of the NEPTUNE array (Figures 2a and S1). Given the optimal locations, we estimate their local magnitudes (ML) by averaging over all the stations in a frequency band of 2-10 Hz (Bakun & Joyner, 1984). The resulting magnitudes, ranging from ML1.6 to ML2.3, are too small to be detected in the ISC catalog (Table S1). For the remaining non-ISC events without clear P and S observations at onshore stations, we use the arrival times of *T*-wave envelope peaks to determine event locations (Figures 2c and S1). Compared to *P*-waves and *S*-waves, *T*-waves are excited within a broad area near the source (Okal, 2008) and consequently less sensitive to earthquake locations, so we limit the grid search to seismically active regions and use a relatively larger interval of 0.05°. Given that oceanic earthquakes are typically shallow and *T*-wave arrival time has little sensitivity to depth, the focal depth is fixed at 10 km. The results suggest that most events reflect local seismicity near the NEPTUNE array (Hyndman et al., 1979; Hooft et al., 2010; Savard et al., 2020) but seven of them are from the Blanco transform fault (Table S1), all of which are consistent with the tectonic background (Figure 2a). We do not determine the magnitudes of the seven Blanco events since a robust magnitude estimate using *T*-wave is challenging (Okal, 2008). However, a previous study by Fox et al. (1993) suggested that detectable *T*-wave events at similar distances are generally of magnitude M2.0+. Overall, our four-day catalog includes many more events compared to the global ISC catalog and provides us with prior knowledge to search for *T*-waves on OOI OBDAS.

## 4 OBDAS for *T*-wave observations and denoising

### 4.1 *T*-wave observations at OOI OBDAS

With the new catalog, we visually scrutinize the *T*-waves on OBDAS for each event at 4-6 Hz, the same frequency band used for the NEPTUNE *T*-wave observations. Most of the events, except for those near the NEPTUNE array, excite visible *T*-waves at OOI North and OOI South (Figure 2; Table S1). In particular, a Mw5.2 Fox islands earthquake, the largest event in our NEPTUNE catalog, generates clear *T*-waves with a duration of >150 s on the 25-60 km portion of OOI North (N25_60) and 20-65 km segment of OOI South (S20_65; Figures 3c and 3d). Intriguingly, the wavefields exhibit a sharp drop of *T*-wave energy at distances of ~60 km on OOI North and ~65 km on OOI South (Figure 3), where the cable orientations become more perpendicular to the *T*-wave propagation direction (Figure 1b). The decreases in *T*-wave energy could be attributed to the directional sensitivity of OBDAS – the radial strain converted from the acoustic pressure of a *T*-wave would be reduced when the incoming wave propagation direction becomes perpendicular to the cable orientation (Martin et al., 2021; Fang et al., 2023). Another possible explanation for the weaker *T*-wave observation could be elevated bathymetry blocking the wave propagation to the seafloor. However, the latter interpretation may not be applicable here as no obvious elevated bathymetry is present. In contrast, earthquakes from the Blanco transform fault exhibit more continuous *T*-wave wavefields across both cables (Figures 3e and 3f), favoring our former interpretation of directional sensitivity. Compared to the Mw5.2 Fox islands earthquake, the

Blanco event produces *T*-waves with shorter durations and lower signal-to-noise ratios (SNR) due to its smaller magnitude (Figure 3). In both cases, *T*-waves consistently exhibit lower SNRs at cable distances less than 30 km (Figure 3), which can be attributed to two main factors. Firstly, the presence of strong background noise associated with ocean gravity waves significantly contaminates the *T*-wave signal. Secondly, as the *T*-wave propagates towards the coast, it undergoes complex interactions with the seafloor, leading to dramatic signal attenuation.

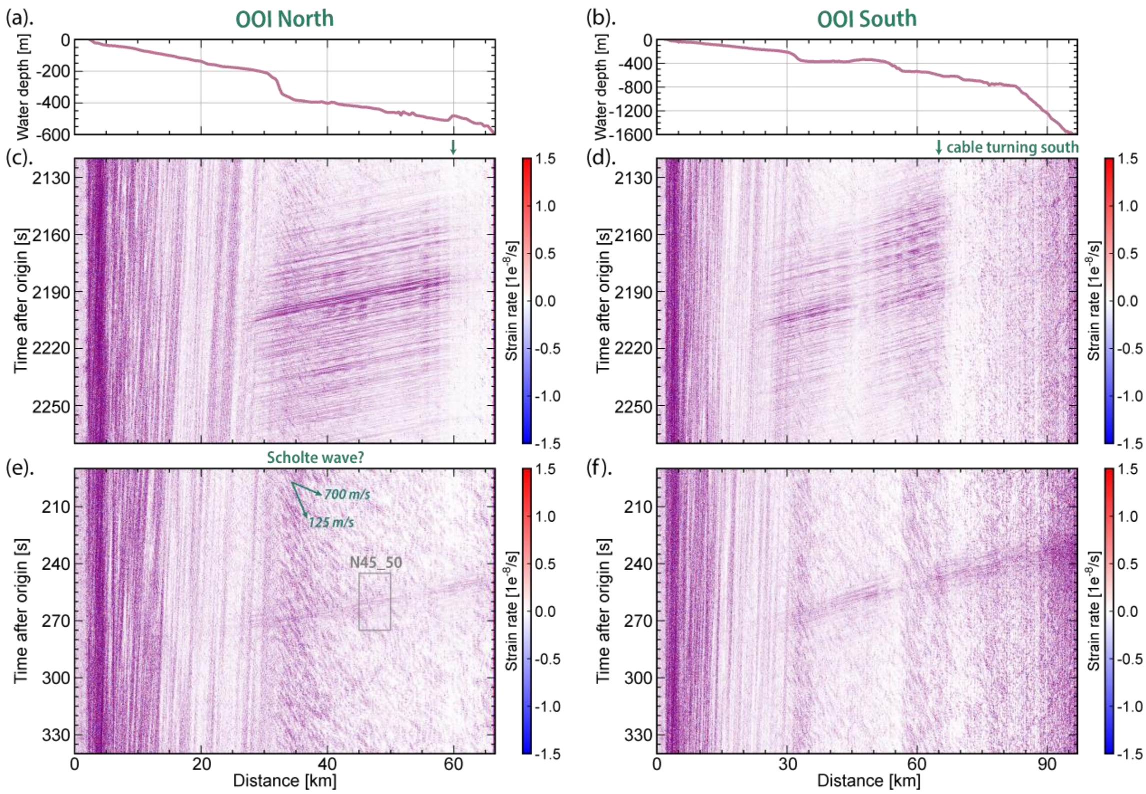


**Figure 3**. 4-6 Hz *T*-waves on the OOI OBDAS arrays. (a). Water depth along OOI North. (b). Water depth along OOI South. (c). The 4-6 Hz *T*-wave on OOI North from the Mw5.2 Fox islands earthquake. (d). Similar to (c) but for OOI South. (e). The 4-6 Hz *T*-wave on OOI North from a Blanco earthquake that occurred on November 4$^{th}$, 2021 (dashed circle in Figure 2a; Event No. 25 in Table S1). The grey box N40_45 denotes the wavefield used in Figures 4 and 6. (f). Similar to (e) but for OOI South.

As a relatively new instrument for underwater environment, OBDAS can in fact record *T*-waves across a broad frequency band, extending beyond the 4-6 Hz range, but with lower SNRs. Taking the Blanco earthquake as an example, we calculate the noise and *T*-wave spectra of individual OBDAS channels on the 45-50 km segment of OOI North (N45_50; Figure 3e). Given a sound speed of 1.5 km/s, we select the noise and *T*-wave windows as -45 to -15 s and -15 to 15 s relative to the predicted *T*-wave arrivals, respectively. The resulting power spectrum density (PSD) of raw OBDAS data exhibits large amplitude noise below 1 Hz, likely associated with ocean-related microseisms (Webb, 1998; Figure 4a). The PSD then sharply drops at 1-2 Hz and gradually decays from 2 Hz to 40 Hz (Figure 4a), which is consistent with previous observations (Lior et al., 2021; Ugalde et al, 2022). The median PSD of the *T*-wave is slightly above the median PSD of noise between 4 Hz and 30 Hz, resulting in a low *T*-wave SNR up to ~3 dB at 10-20 Hz (Figure 4). OOI South also exhibits similar *T*-wave observations, while the NEPTUNE OBS at a similar water depth but a larger distance shows one order of magnitude higher SNRs over a broad frequency range (2-40 Hz) peaking at 3-5 Hz (Figure 4b). The low SNRs in OOI OBDAS are due to significant noise masking the landward propagating *T*-wave. The noise is predominantly grouped in the seaward direction with a slowness range of 125-700 m/s, which is likely associated with Scholte waves backscattered from a bathymetry step at ~30 km on OOI North (Figure 3e). Previous OBDAS studies also reported backscattered Scholte waves in ambient noise cross-correlations and attributed them to subsurface lateral variations (Spica et al., 2020; Cheng et al., 2021). Here, our observations of backscattered Scholte waves are likely linked with the sharp change of bathymetry as supported by their consistent presence on both OOI OBDAS arrays (e.g., ~30 km and ~60 km at OOI South; Figure 3).

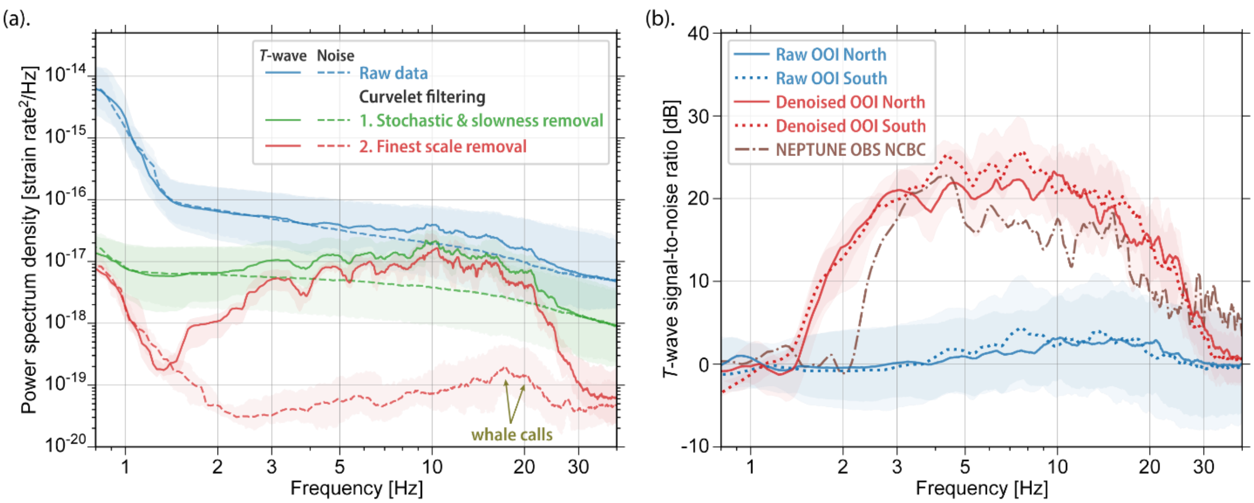


**Figure 4**. Power spectral density and SNR of a *T*-wave at the OOI OBDAS and a NEPTUNE OBS station. (a). Strain rate PSD of raw data and curvelet filtered data at N45_50. The solid lines denote the median PSDs of a *T*-wave across N45_50. The dashed lines correspond to the median PSDs of noise. The curves are color-coded to display the outcomes resulting from successive curvelet denoising steps. The shadow areas represent the 10th to 90th percentiles of corresponding PSDs obtained from individual channels at N45_50. (b). *T*-wave SNRs at OOI North (N45_50), OOI South (S50_55), and NEPTUNE station NCBC as a function of frequency. The SNR curves plotted for OBDAS represent the median SNRs of individual channels. The associated shadow areas correspond to the 10th to 90th percentiles of PSDs obtained from individual channels. N45_50, S50_55, and NCBC are at a similar water depth of ~400 m.

### 4.2 Curvelet denoising

We adopt a curvelet denoising approach to enhance *T*-wave SNRs by taking advantage of waveform coherence across dense OBDAS channels. Curvelets are designed to optimally represent images with a finite number of geometric discontinuities along twice continuously differentiable curves, which is a desirable tool for DAS data with the *T*-wave acting as bounded curvature (Candès & Donoho, 2004). Compared to classic Fourier and wavelet transforms, the curvelet transform is a tight frame that enables the reconstruction of an image with a series of curvelets weighted by their coefficients but is better suited to preserving directional features through a polar tiling of the frequency-wavenumber (f-k) domain (Candès et al., 2006). For practical applications with discrete data (e.g., OBDAS seismic data), the curvelet transform is usually implemented in a discrete frame using Cartesian counterparts of the polar tiling. Explicitly, the f-k plane is partitioned into a range of concentric scales dictated by dyadic squares whose width doubles every scale (Figure 5). Each scale is further compartmentalized by slowness into a set of parabolic angular wedges, which correspond to needle-shaped wave packets or mother curvelets in the time domain (Figure 5). Due to the parabolic scaling, the number of wedges doubles every other scale, and the mother curvelets consequently become more needle-like at finer scales. In this manner, the curvelet transform presents a high degree of localization in position, frequency, and orientation, and thus has been exploited in seismology for seismic denoising (Hennenfent & Herrmann, 2006), wavefield reconstruction (Jack & Zhan, 2021), and seismic phase augmentation (Yu et al., 2017; Zhang & Langston, 2020).

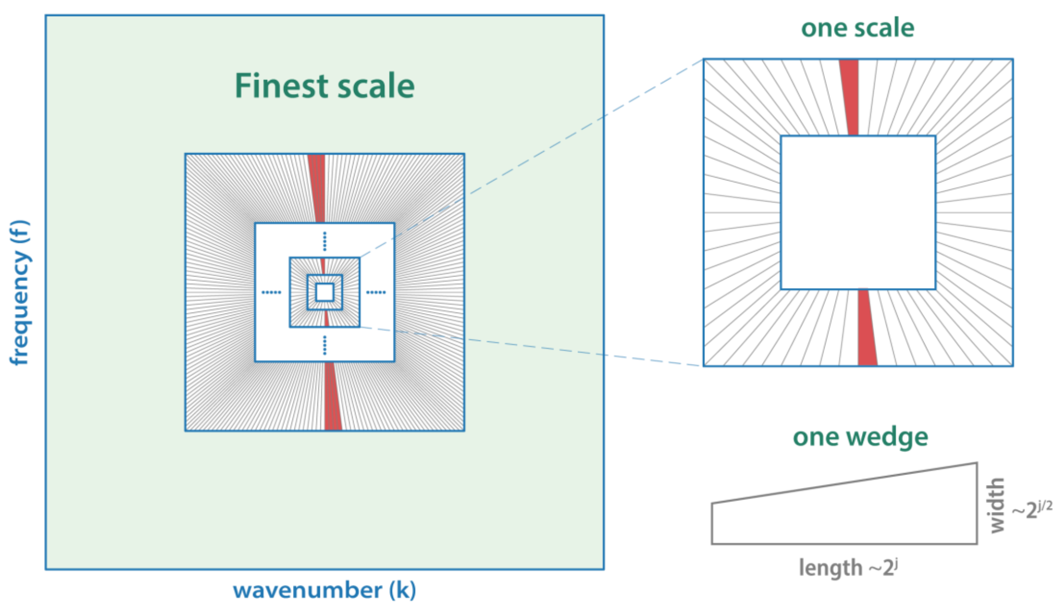


**Figure 5**. Schematic curvelet tiling of the frequency-wavenumber domain. The right panels are examples of the third scale and a parabolic angular wedge. Red wedges denote the wedges associated with *T*-wave slowness and thus are retained during the slowness removal.

Recently, Atterholt et al. (2022) proposed a unified wavefield-partitioning approach for simultaneously removing stochastic and coherent noise (e.g., traffic signals) for DAS on land. Under the curvelet frame, stochastic noise can be removed by implementing a soft thresholding to curvelet coefficients, which involves zeroing the curvelet coefficients below a noise threshold and subtracting the threshold from those above it. The effect of slowness removal for coherent noise is to mute angular wedges associated with the noise slowness. We follow a similar scheme and apply stochastic and slowness removal to OOI North for the Blanco example. We adopt a wrapping-based fast discrete curvelet transform algorithm for computational efficiency and assign wavelets to facilitate the implementation of appropriate basis functions at the finest scale (Candès et al., 2006). Unlike DAS on land, the noise level and *T*-wave energy of OBDAS exhibit significant lateral variation dependent on water depth and bathymetry (Figure 3). Therefore, we implement a spatially dependent soft thresholding by taking cable location into account. Specifically, we cut a 180-s window before the *T*-wave arrival as a noise window and take the curvelet transform of it. For each curvelet, its coefficient matrix describes the corresponding noise level in both temporal and spatial dimensions. By rolling along the cable, we set the threshold as the 70th percentile of the coefficient matrix at each cable location. In slowness removal, we only retain the curvelets associated with *T*-waves propagating towards the shore at an apparent speed faster than ~1.0 km/s. Indeed, the stochastic and slowness removal improves *T*-wave SNRs at individual channels and suppresses the coherent noise moving seaward (Figures 6a/6d vs 6b/6e). Consequently, the median PSD of the stochastic and slowness filtered *T*-wave exceeds the noise level at low frequencies (e.g., 2-4 Hz; Figure 4a).

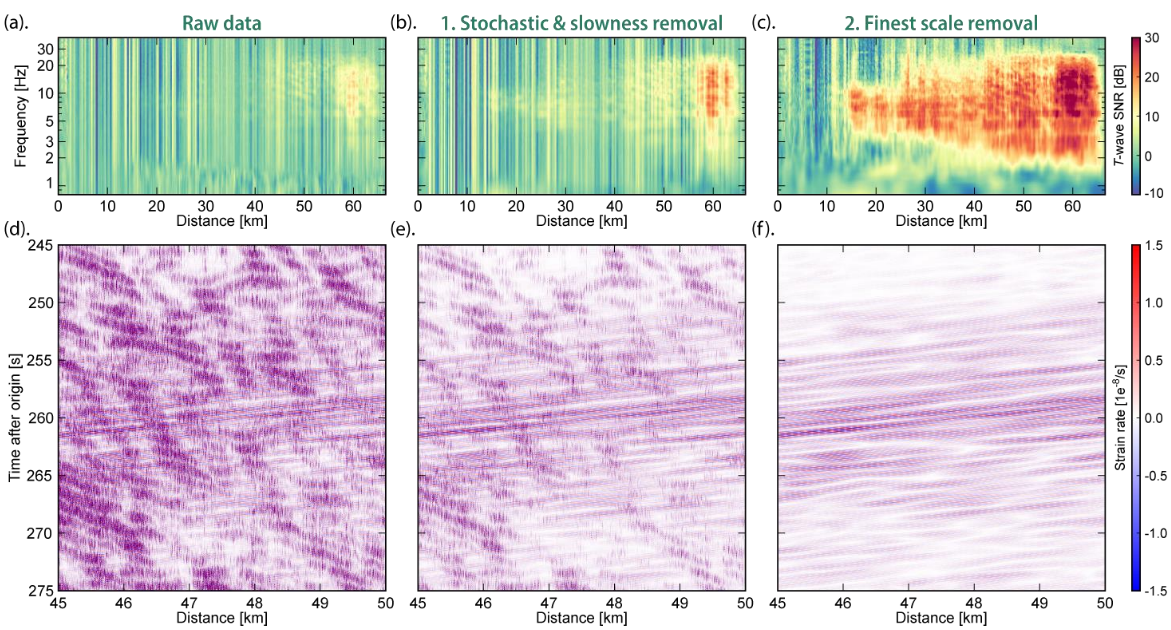


**Figure 6**. Illustration of curvelet denoising for enhancing *T*-wave SNRs on OBDAS. (a). *T*-wave SNRs of individual OBDAS channels in OOI North. (b). *T*-wave SNRs after stochastic denoising and slowness removal. (c). *T*-wave SNRs after an additional finest-scale removal. (d). The 4-6 Hz

OBDAS wavefield at N45_50 in Figure 3e. (e). The 4-6 Hz OBDAS wavefield after stochastic and slowness removal. (f). Similar to (e) but after an additional finest-scale removal.

Despite the application of stochastic and slowness denoising, there is certain spiky noise in the data that cannot be effectively removed. The spiky noise demonstrates very low coherency and, therefore, unlikely corresponds to *T*-waves or any natural signals (Figure 6e). Upon thorough examination, we find that these spiky artifacts are primarily concentrated in the finest scale of the f-k domain. Thus, to further improve *T*-wave SNRs, we implement an additional finest-scale removal approach by zeroing out all the coefficients at finest scale (Figures 6c and 6f). As a result, the median PSD abruptly drops to ~$10^{-19}$, which is 2-3 orders of magnitude smaller than that of the original data (Figure 4a). Intriguingly, we observe that a small PSD peak emerges around 20 Hz in our noise time window, which has been suggested to be associated with whale calls (Wilcock et al., 2023; Figure 4a). After denoising, the median *T*-wave SNRs of OOI North and OOI South can reach up to ~25 dB over a broad frequency band spanning from 1.5 Hz to 30 Hz, slightly outperforming a NEPTUNE OBS at a similar water depth (Figure 4b).

## 5 OBDAS for oceanic seismicity detection and location

### 5.1 detecting *T*-wave events

Curvelet denoising effectively enhances *T*-wave signals, enabling us to detect small *T*-wave events hidden in the noise. To illustrate, we select two representative events from the NEPTUNE *T*-wave catalog (i.e., Event No. 5 and 27 in Table S1). The first event with a small magnitude of ML1.7 occurred near the Explorer ridge, which is about 460 km away from OOI North. The other event at the Blanco transform fault is at a shorter distance of ~240 km. We apply the recursive STA/LTA algorithm to detect *T*-waves in a frequency band of 5-10 Hz on the 40-60 km segment of OOI North (N40_60), which has relatively high SNRs along the cable (Figure 3). However, both events are too small to produce detectable *T*-wave signals in the raw data. Consequently, the STA/LTA approach fails to trigger a detection for the *T*-wave (Figures 7a and 7c), except for a small portion of the cable (e.g., at ~50 and ~60 km) where STA/LTA amplitudes slightly are higher than the background levels at the predicted *T*-wave arrival times of the Blanco event (Figure 7c). After denoising, *T*-waves become evidently visible across N40_60 for both events (Figures 7b and 7d), underscoring the great seismic monitoring potential of OBDAS. In addition, curvelet denoising also substantially enhances the *P*-wave from the Blanco earthquake while the *S*-wave remains undetected (Figure 7d).

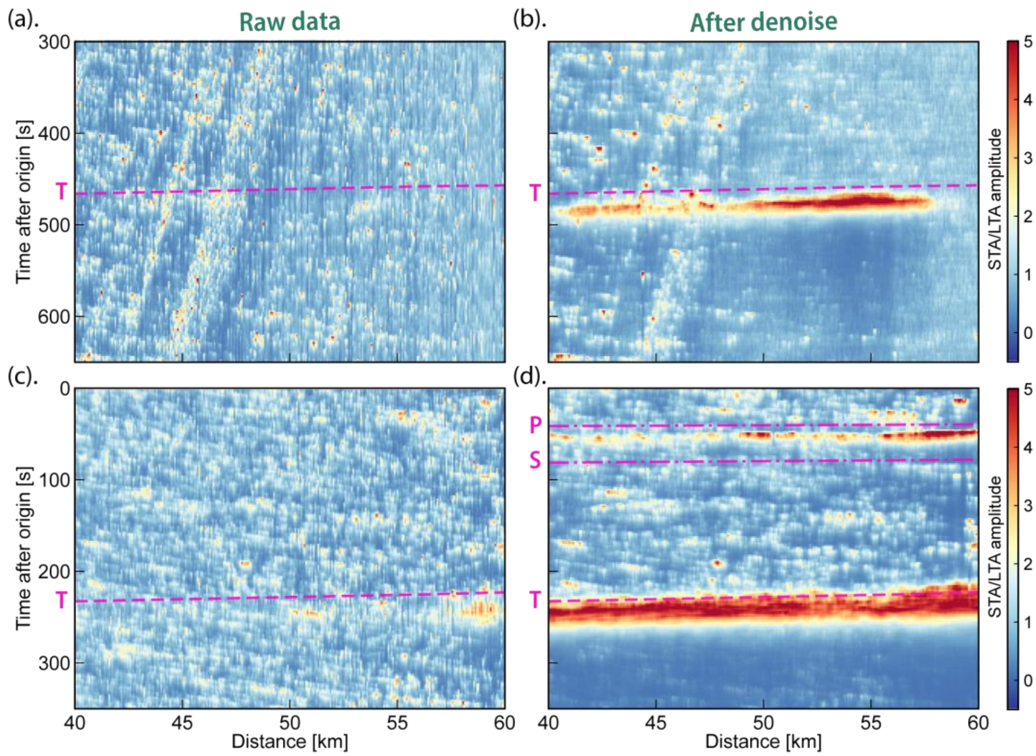


**Figure 7**. Illustration of curvelet denoising for enhancing *T*-wave detectability of OBDAS. (a). STA/LTA results for 5-10 Hz raw OBDAS data of the ML1.7 earthquake on November 2nd, 2021 (Event No. 5 in Table S1). (b). Similar to (a) but for denoised data. (c). STA/LTA detections using 5-10 Hz raw OBDAS data of the Blanco earthquake on November 5th, 2021 (Event No. 27 in Table S1). (d). Similar to (c) but for curvelet denoised data.

The evident effectiveness of curvelet denoising in these two small earthquakes motivates us to investigate the potential of OBDAS for long-term *T*-wave detection. We use the complete 4-day dataset of N40_60, downsample the data to 50 Hz, divide them into 10-min windows, and apply curvelet denoising and recursive STA/LTA. We average the STA/LTA over all channels with a velocity correction of 1.5 km/s. An event is detected if the averaged STA/LTA amplitude exceeds a threshold of 1.5, similar to the NEPTUNE *T*-wave catalog. After visual scrutinization to remove *P*-waves and false detections, we document a total of 92 *T*-wave events for OOI North. Compared to the NEPTUNE *T*-wave catalog, our new OOI North *T*-wave catalog includes 17 of the 27 NEPTUNE events. The missed 10 events are local seismicity near the NEPTUNE array (gray circles in Figure 2), which are probably too small to be detected at OOI North. Meanwhile, OOI North identifies 2-3 times more earthquakes than the NEPTUNE array in the first half of the experiment (Figure 8). The excess *T*-wave events on OOI North are likely associated with aftershocks of a mb3.9 Blanco earthquake or a mb3.4 Blanco earthquake that both occurred on November 1$^{st}$, 2021 (Figure 9), right before the experiment. The *T*-wave detection rate of OOI North gradually decreases from 6-8 events per 4 hours on November 2$^{nd}$ to 1-4 events per 4 hours on November 4$^{th}$ and 5$^{th}$. This declining trend could be partially attributed to an increase in the noise level starting on November 4th (Figure 8). A likely decrease in aftershock productivity may also contribute to the reduced detections but we lack independent observations to support this interpretation.

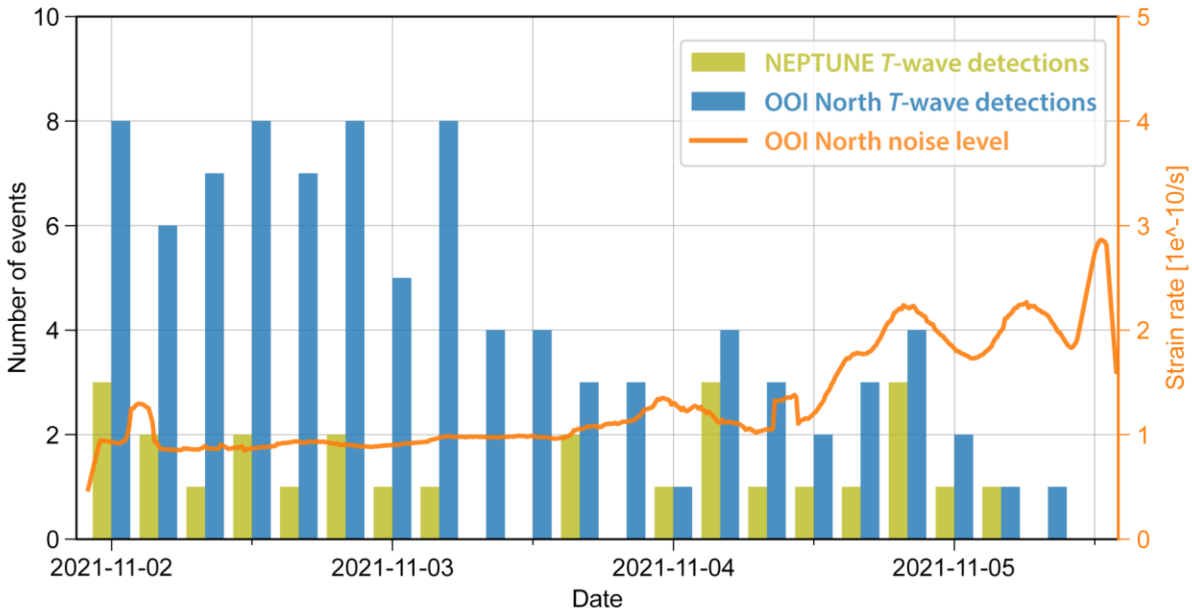


**Figure 8.** Comparison of detection rates *T*-wave events on OOI North and NEPTUNE array. The orange curve of noise level on OOI North starts to increase on November 4th, 20021.

The significantly higher number of *T*-wave event detections on OOI North compared to the NEPTUNE network highlights the potential of OBDAS for long-term oceanic seismicity monitoring, though the comparison may be not entirely fair given their different instrument locations. In spite of large uncertainty, a straightforward linear extrapolation based on the 92 detections observed over a 4-day period suggests a potential annual detection rate of approximately 8000 events. Using U.S. Navy SOSUS hydrophones, Fox et al. (1993) reported an annual detection of 1000-2000 events in the Juan de Fuca region and established a Gutenberg-Richter law with a b-value of 1.42. Based on their model, our extrapolation of ~8000 events per year implies that OOI OBDAS can detect regional seismicity with a minimum magnitude of mb1.4.

### 5.2 Constraining the source azimuth of Blanco earthquakes

Even though retrieving a complete source location from *T*-waves recorded at one site is challenging, the cable directionality of OOI OBDAS enables us to estimate the back azimuth of regional Blanco earthquakes through array beamforming. For instance, assuming earthquakes occurred tightly along the Blanco transform fault trace (Kuna et al., 2019), we calculate the predicted *T*-wave arrival times along the OOI North cable for five equally spaced events using a constant sound speed of 1.5 km/s (Figure S2). The cable geometry alteration at cable distance of 55 km yields apparently distinct slope patterns of the *T*-wave arrival time curves (Figure S2). Specifically, within the <55 km cable section, more pronounced disparities in apparent velocity slopes are observed compared to the cable section beyond 55 km (Figure S2). This implies that the <55 km cable section exhibits higher sensitivity to azimuthal constraints of Blanco events. Therefore, we choose the N40_55 km segment—a region marked by high sensitivity to source location and high *T*-wave SNRs—to compute the apparent velocity and infer the back azimuth of a Blanco event detected by OBDAS.

Indeed, the theoretical *T*-wave arrival times along the N40_50 segment from Blanco earthquakes unveil a discernible pattern of location-dependent apparent velocity (Figures 9). The apparent velocity gradually increases from 1.5 km/s to 5 km/s as an earthquake moves eastward along the Blanco transform fault (Figure 9), allowing for source azimuth estimation. Taking a Blanco event that occurred at 00:05 on November 2nd, 2021, as an example, a slant stack of its *T*-waves at N40_55 exhibits an amplitude peak at an apparent velocity of 1.82 km/s, which corresponds to a back azimuth of 252° given a propagation speed of 1.5 km/s (Figure 9). The resolved back azimuth intercepts the Blanco fault trace at a location of 44.08°N, 129.17°W. The Blanco example is close to our relocated mb3.4 Blanco event that occurred at 2021-11-01T12:59, right before the OOI community experiment, suggesting that it could be an aftershock of the mb3.4 event. With this location, we calculate the theoretical *T*-wave arrival times at two NEPTUNE stations, which align reasonably well with observed data (Figure S3). Meanwhile, compared to the mb3.9 and mb3.4 events, the *T*-wave amplitudes of our Blanco event example are one order of magnitude weaker at the same station (Figure S3), indicating a relatively small magnitude. However, only OOI North is used in this example, leaving the epicenter distance unresolved. Looking forward, an optimal approach to determine the source location would involve integrating travel time and slowness data from all available instruments, including OBDAS, *T*-wave stations, and hydrophones from a wide range of azimuths.

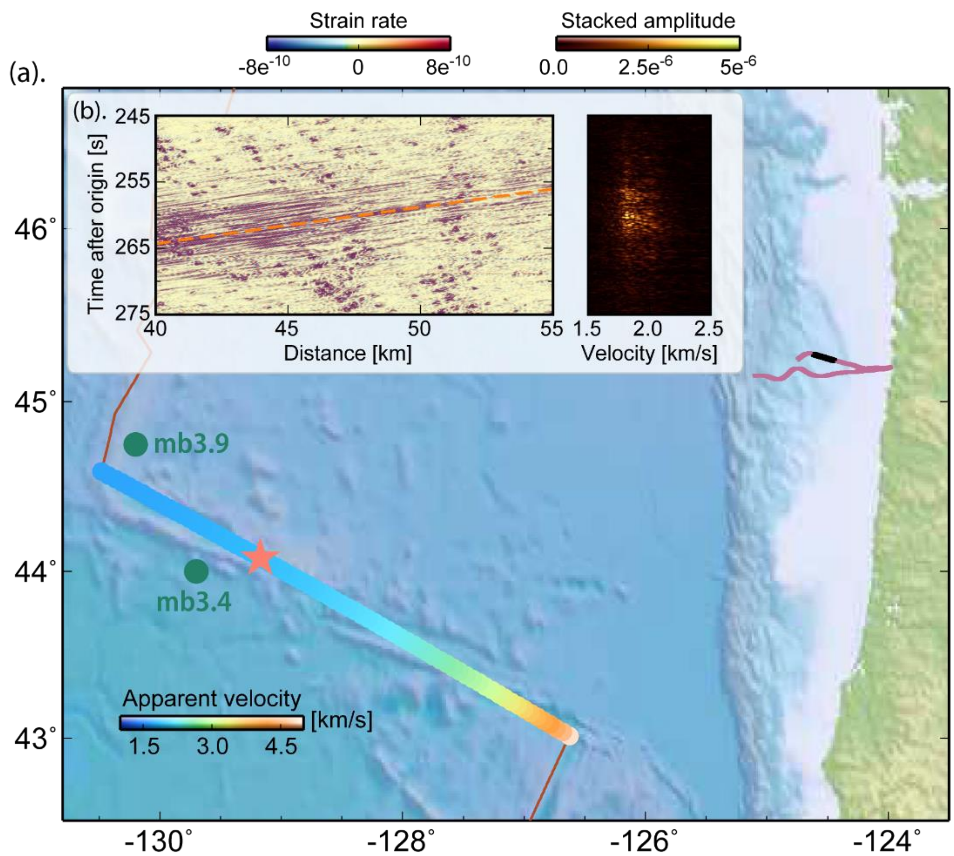


**Figure 9.** Locating the 2021-11-02T00:05 Blanco earthquake using *T*-waves on OOI North. (a). Slowness sensitivity of OOI North *T*-wave to earthquake location. The color along the Blanco transform fault shows predicted *T*-wave slowness at N40_55 (black line), corresponding to different earthquake locations along the fault. The green circles and red star denote the relocated mb3.9, mb3.4 and estimated location of the 2021-11-02T00:05 event, respectively. (b). *T*-waves at 5-10 Hz and slant stack results. The orange dashed line represents the *T*-wave apparent velocity of 1.82 km/s.

## 6 OBDAS for seismic ocean thermometry

The improved SNRs of *T*-waves through denoising also helps enhance the feasibility of OBDAS-based seismic ocean thermometry, allowing a larger number of small repeating earthquakes to be employed for SOT. In the Northeast Pacific, the abundant seismicity along the Aleutian subduction zone can generate high-quality *T*-waves propagating to the OOI OBS array. Following Wu et al. (2020), we identify two repeating earthquakes, on June 15$^{th}$, 2016 and January 7$^{th}$, 2018, near the epicenter of the Mw5.2 Fox Islands earthquake. They exhibit almost identical *P*-waves at four local stations (Figure 10c). The corresponding *T*-waves at OOI OBSs HYS11-14 also show high cross-correlation (CC) coefficients of ~0.90 in a frequency band of 2.5-3.5 Hz (Figure 10e). The CC coefficient gradually drops as the frequency increases (Figure 10d), that is similar to the previous observations in the Indian Ocean (Callies et al., 2023; Wu et al., 2023). Taking a CC coefficient threshold of 0.6, the *T*-wave travel time shifts between 2.35 Hz and 4.6 Hz would be used to infer average ocean temperature change along the *T*-wave path. In this example, the slight *T*-wave travel time shift of -0.04 s at 3 Hz (Figure 10d) indicates a weakly warming ocean averaged over the top 3 km of the water column along the ~3000 km source-receiver path (see supplementary text S2 and Figure S4 for more details; Komatitsch & Tromp, 1999; McDougall & Barker, 2011; Forget et al., 2015).

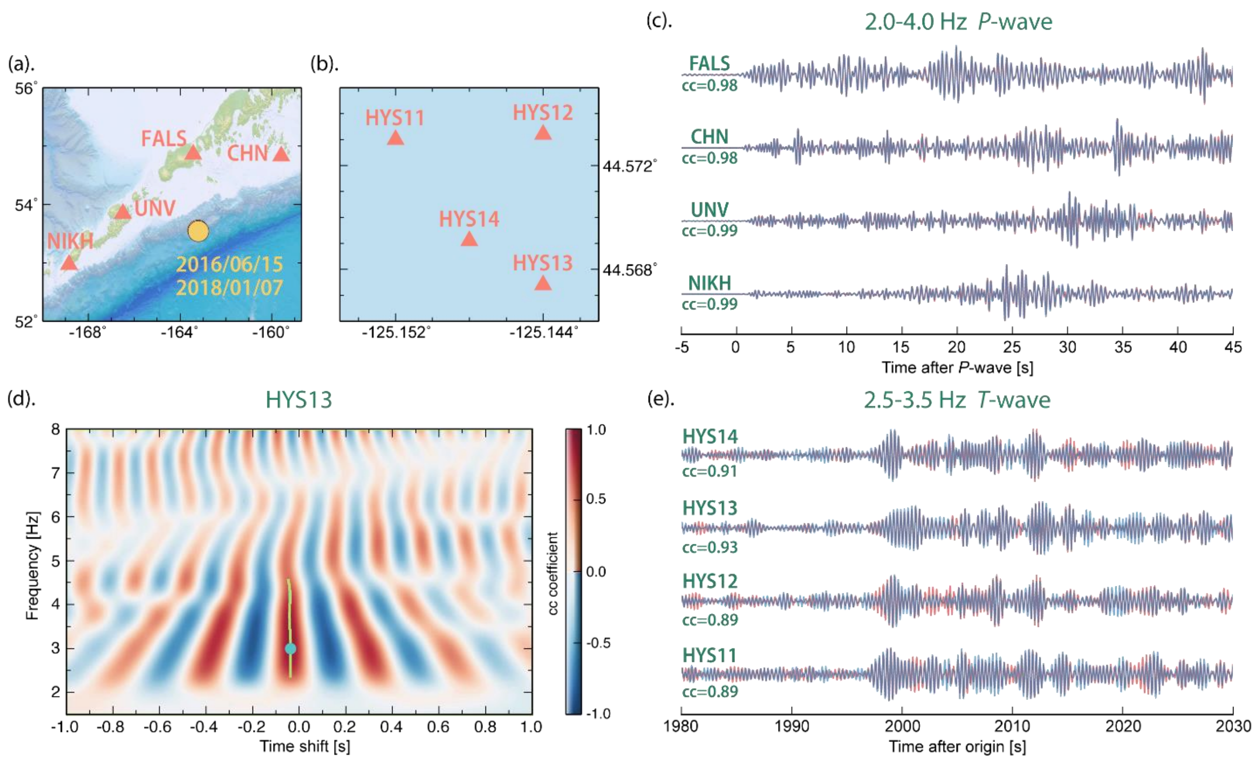


**Figure 10.** Illustration of SOT concept using repeating earthquakes in the Aleutian trench and OOI OBSs. (a). The map of repeating earthquakes and local stations at the Aleutian trench. (b). The map of OOI OBS array. (c). *P*-waves of the 15 June 2016 event (red) and 7 January 2018 (blue) event. The station names and CC coefficients are indicated on the left. *P*-waves from the 2016 event are synchronized based on their predicted arrivals at each station using the ISC source parameters. The *P*-waves from the 2018 event are aligned with the corresponding 2016 *P*-waves using waveform cross correlation. (d). Frequency dependent *T*-wave CC results of HYS13. The green line indicates the frequency-dependent time shifts measured by tracking the stripe of peak CC coefficient above 0.6. The green dot shows a time shift of -0.04 s measured at 3 Hz. (e). *T*-waves at the four OOI OBSs. The relative origin time error between the 2016 event and 2018 event is corrected using the *P*-waves shown in (c).

Within the limited 4-day experiment period, we do not find any natural repeating earthquake pair in the Northeast Pacific region producing *T*-waves usable for SOT. Thus, we generate pseudo-repeating earthquakes to evaluate the SOT performance of OBDAS by incorporating realistic noise data into the *T*-waves of the Mw5.2 Fox Islands earthquake. Specifically, we randomly select 20 three-minute noise data segments from OOI North and superimpose each of these noise segments onto magnitude-calibrated *T*-waves. To perform the calibration, we assume a circular crack model and constant stress drop (Madariaga, 1976; Allmann & Shearer, 2009). Based on this assumption, the *T*-wave amplitude would be proportional to $M_o^{2/3}$, where $M_o$ represents the seismic moment. For instance, a decrease in the moment magnitude by one-unit results in a 10-fold drop of *T*-wave amplitude. With the scaling, we generate pseudo-repeating OBSDAS *T*-waves for a given magnitude, perform curvelet denoising, and evaluate the performance of OBSDAS for SOT. We use the OBDAS data at N40_60 for illustration. It is important to point out that applying stochastic removal independently to each pseudo-repeating event can lead to inconsistent zeroing of noisy curvelet coefficients and compromise the accuracy of *T*-wave time shifts. To ensure a consistent and unbiased treatment of the repeating *T*-waves, we identify and remove the overlapping noisy curvelet coefficients for each given pair in the curvelet denoising.

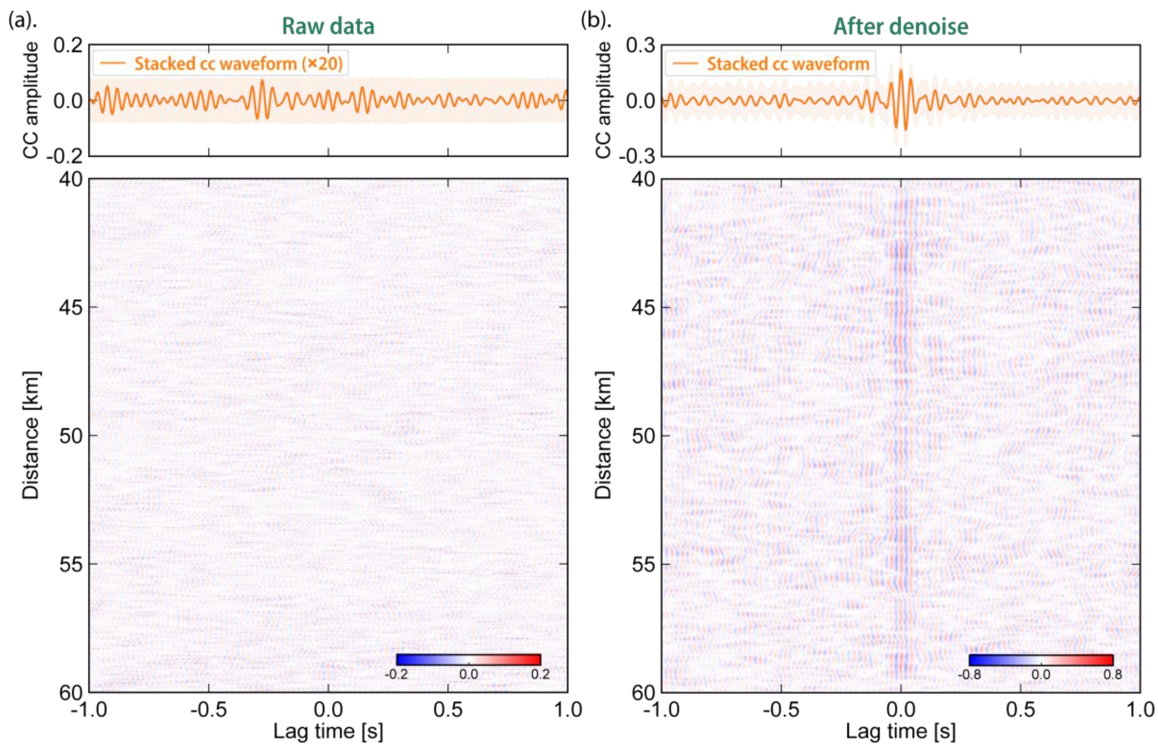


**Figure 11.** Illustration of improved CCs with curvelet denoising of OBDAS Data. (a). Raw *T*-wave CCs between two Mw3.5 pseudo-repeating earthquakes at 3-5 Hz. The top panel presents the stacked CC (multiplied by 20 for better visualization), the orange shadow area denotes the 10th-90th percentile of individual CCs. (b). Similar to (a) but for denoised *T*-waves.

As an example, we generate two M3.5 pseudo-repeating earthquakes by downscaling the *T*-waves from the Mw5.2 Fox Islands earthquake with a factor of 50. We cut the two repeating *T*-waves with a 60-s time window and cross correlate them at individual OBDAS channels. However, the *T*-wave signals are so weak relative to the noise that no coherent CC signals are observed (Figure 11a). The stacked CC waveform exhibits a weak peak at a time shift of -0.27 s, substantially deviating from the input value of 0.0 s. In contrast, curvelet denoising greatly enhances the *T*-wave, resulting in coherent CC signals that are visible on most channels. The coherent signal is further enhanced in the stacked CC waveform with a clear peak amplitude at 0.0 s, matching the expected input number (Figure 11b). Here, we first cross correlate individual *T*-waves and subsequently stack the resulting CCs to accommodate potential waveform variations among different channels. Conversely, stacking array waveforms prior to the cross-correlation step may lead to destructive interference of *T*-waves, compromising the accuracy of the measurements.

To ensure robustness, we repeat this M3.5 repeater analysis using all the selected 20 noise windows, which yields a total of 190 pseudo-repeating earthquake pairs. We successfully retrieve the expected time shift of 0.00 s across all pairs, with an error margin of less than 0.02 s corresponding to our downsampled time interval (Figure 12a). Furthermore, we extend the M3.5 scenario to a wide range of earthquake magnitude, spanning from M2.7 to M4.1 with an interval of M0.1. Curvelet denoising evidently reduces the magnitude required for reliable time shift measurements (Figure 12a). Taking a criterion of >99% pairs with successful time shift retrieval (i.e., SOT robustness >0.99 in Figure 12a), the magnitude threshold decreases from M4.0 to M3.5. Based on the Gutenberg-Richter law (Gutenberg & Richter, 1944), a decrease in magnitude threshold by M0.5 would result in a roughly threefold increase in the count of usable repeating events. Additionally, the quadratic relationship between the number of repeaters and repeating pairs indicates a potential order of magnitude increase of repeating pairs.

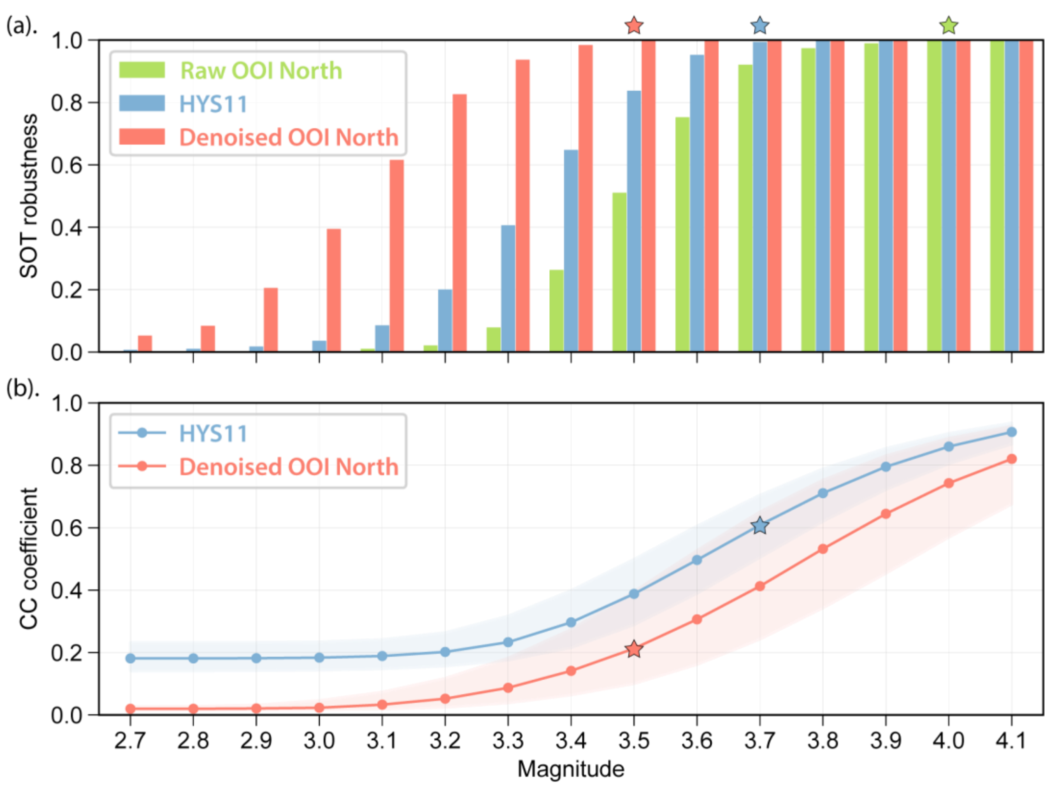

**Figure 12.** Comparison of SOT performance between OBDAS and OBS. (a). SOT robustness using HYS11 data, raw OOI North data, and denoised OOI North data, as a function of earthquake magnitude. The SOT robustness is indexed by the ratio of successful pairs, where the input travel time shift of 0.00 s is accurately recovered, to the total number of repeating pairs. The stars indicate magnitude thresholds, above which >99% pairs accurately retrieve the time shift. (b). CC peak amplitudes using HYS11 and denoised OOI North data, as a function of earthquake magnitude. The blue represents the median of CC peak amplitudes among the 1400 repeating pairs for HYS11. The red line shows the median of stacking CC amplitude peaks among the 190 repeating pairs for OOI North. The shadow area indicates the 10th-90th percentiles.

We also attempt to evaluate the SOT performance of a neighboring OBS station, specifically HYS11, for a comparison with OBDAS (Figure 1). However, during the community experiment, HYS11 was inactive for maintenance and did not record the *T*-wave from the M5.2 Fox island earthquake. To address the issue, one could involve another M5.2 earthquake recorded by HYS11 or a different magnitude earthquake with magnitude calibration. However, such an approach can introduce substantial uncertainty due to the complex nature of *T*-wave excitation, where even slight differences in source parameters can affect *T*-wave amplitudes and thus lead to calibration biases. Therefore, we opt not to solely rely on the simplistic calibration method. Alternatively, we leverage the NEPTUNE dataset, which captures earthquakes during, after and prior to the experiment, to establish a reliable calibration relation between OBDAS and HYS11 (see supplement material text S3 for details; Figure S5). Using NEPTUNE as a reference, the calibration method effectively cancels out complex effects arising from differences in source parameters and bridges a direct comparison between OBS and OBDAS. Similar to the aforementioned evaluation for OBDAS, we generate pseudo-repeating pairs for HYS11 by utilizing seven Mw5.0+ Fox islands earthquakes (Figure S6) and 200 randomly selected noise waveforms. With a total of 1400 pseudo-repeating pairs, the magnitude threshold for HYS11 is M3.7, higher than the threshold of M3.5 for OBDAS (Figure 12a). This magnitude difference indicates that using OBDAS can potentially provide four times more small repeating pairs for SOT compared to OBS. However, it is important to note that our comparison is influenced by the noise level of OBDAS. The current 4-day OBDAS data show large variations in noise levels (Figure 8), indicating that long-term OBDAS observations are required for a robust quantification. In addition, our estimated magnitude threshold for SOT can vary substantially depending on the region and the earthquake source parameters, as *T*-wave excitation is strongly modulated by bathymetric features in different regions, resulting in varying SNRs of the *T*-wave (de Groot-Hedlin & Orcutt, 2001).

In practical SOT applications, a CC coefficient threshold is typically used to ensure accurate *T*-wave time shift measurements. Previous studies using *T*-wave stations and hydrophones have established an empirical threshold of 0.6 based on visual examination of the CC waveforms, lacking a solid justification (Wu et al., 2020). Intriguingly, our pseudo-repeating tests show that the median of CC peak amplitudes for HYS11 corresponds to 0.6 at the magnitude threshold of

M3.7 (Figure 12b), supporting the previous choices. For OBDAS data, a lower threshold, such as 0.2 for OOI North, can be adopted benefiting from stacking of multiple channels.

## 7 Discussion: Noise in OBDAS data

The noise level in OBDAS data is a critical parameter affecting the *T*-wave data quality. During the four-day experiment, the OBDAS noise level gradually increased by a factor of 1-2. The source of OBDAS noise and its temporal variability remain unclear. Analysis of previous OBS data indicates that tilt and compliance processes are major contributors to OBS noise, both of which are associated with ocean dynamics (Hilmo & Wilcock, 2020; Janiszewski et al., 2022). While OBDAS and OBS operate on distinct principles for vibration sensing, their noise sources are not necessarily identical. Nevertheless, we do observe fluctuations in ocean wave height and wind direction within the four-day period (Hersbach et al., 2023), suggesting a potential link between OBDAS noise and ocean dynamics (Figure S7). However, such correlation is still inconclusive due to limited 4-day data.

To evaluate the effect of varying noise on SOT, we randomly select 20 noise samples each from the first and last 24 hours, representing low and high noise levels, respectively. Consequently, the magnitude threshold for high-quality SOT increases from M3.2 at low noise level to M3.6 at high noise level (Figure S8a). Nonetheless, the corresponding median of CC peak amplitudes for both scenarios consistently fall within the range of 0.1-0.2, reinforcing that a CC coefficient threshold of 0.2 could be suitable for SOT using a 20-km OBDAS cable regardless of noise level (Figure S8b). Meanwhile, in previous sections, we use a fixed threshold of 70th percentile noise level for the stochastic removal. Given the temporal variability of OBDAS noise levels, one may adjust the threshold for better denoising. Yet, our tests indicate that varying the threshold within the 50th-100th percentile range barely affects the SOT performance – only the 90th percentile threshold case marginally outperforms the others (Figure S9). However, our assessment strongly relies on current dataset and might not be generalized to other OBDAS datasets.

Although curvelet denoising efficiently reduces noise, the exact sources of the noise remain unknown. In particular, the strong incoherent spiky noise is ubiquitous in the OBDAS data (Figure S10). It often accompanies ocean gravity waves and becomes most pronounced around the peaks and troughs of these waves (Figure S10). Its amplitude generally increases at shallower water depths (Figure S10). Intriguingly, higher noise levels in shallower water have also been reported in OBS data, which are attributed to the seafloor compliance effects due to orbital motions of ocean waves (Hilmo & Wilcock, 2020; Janiszewski et al., 2022). The spiky noise in OBDAS data also shows a similar depth dependency, although its exact mechanism remains mysterious. Thus, further investigations with more data from diverse ocean environments are warranted to better understand the characteristics and sources of OBDAS noise.

## 8 Conclusions

In this study, we investigate the performance of OBDAS for oceanic seismicity detection and SOT using the 4-day data collected from the OOI cables offshore central Oregon. To do so, we first develop a curvelet denoising that effectively enhances *T*-wave signals. This scheme includes stochastic noise removal, slowness removal and finest-scale removal for different types of noise. Our results demonstrate that curvelet denoising effectively enhances *T*-wave signal, resulting in a substantial improvement of *T*-wave event detectability. After denoising, we identify 92 oceanic events on OOI North, which is three times more than the NEPTUNE catalog. However, the *T*-wave detectability of OOI North decreases due to a higher noise level during the latter half of the experiment, highlighting the influences of noise variations. The sensor density and cable directionality of OBDAS enables us to constrain the source azimuth of regional oceanic seismicity. We also evaluate the SOT feasibility of OBDAS and juxtapose its performance with conventional OBSs. To evaluate the feasibility, we synthesize *T*-waves of pseudo-repeating earthquakes using the observed *T*-waves from a Mw5.2 Fox Islands earthquake and background noise recorded by OOI OBDAS. Our findings show that OOI OBDAS, leveraging its array data advantage, can record *T*-waves from a ~3000 km distant repeating earthquake, with a magnitude >M3.5, suitable for SOT. In contrast, using OBS requires a slightly higher magnitude threshold of M3.7. However, the performance of OBDAS for oceanic seismicity detection and SOT highly depends on both natural and instrumental noise levels, which awaits further investigation.

## Acknowledgments

We are grateful for the constructive discussions with Daniel Lizarralde and John A Collins. This project is supported by the Woods Hole Oceanographic Institution Independent Research & Development Program. We thank the high-performance computing resources at Woods Hole Oceanographic Institution made available for conducting this research. Z. S. also acknowledges the support of the Weston Howland Jr. Postdoctoral Scholarship.

## Open Research

The curvelet code is available on the curvelet.org website (http://www.curvelet.org) and https://github.com/atterholt/curvelet-denoising. The OOI RCA community experiment OBDAS data is available from http://piweb.ooirsn.uw.edu/das/. The ocean wave height and wind speed data are downloaded from Copernicus Climate Change Service Climate Data Store (10.24381/cds.adbb2d47).

**References**


Allmann, B. P., & Shearer, P. M. (2009). Global variations of stress drop for moderate to large earthquakes. *Journal of Geophysical Research: Solid Earth*, *114*(B1).

ATOC Consortium. (1998). Ocean climate change: Comparison of acoustic tomography, satellite altimetry, and modeling. *Science*, *281*(5381), 1327-1332.

Atterholt, J., Zhan, Z., Shen, Z., & Li, Z. (2022). A unified wavefield-partitioning approach for distributed acoustic sensing. *Geophysical Journal International*, *228*(2), 1410-1418.

Bakun, W. H., & Joyner, W. B. (1984). The ML scale in central California. *Bulletin of the Seismological Society of America*, *74*(5), 1827-1843.

Barnes, C. R., Best, M. M., & Zielinski, A. (2008). The NEPTUNE Canada regional cabled ocean observatory. *Technology (Crayford, England)*, *50*(3).

Bondár, I., & Storchak, D. A., (2011). Improved location procedures at the International Seismological Centre. *Geophys. J. Int.*, 186, 1220-1244

Buehler, J. S., & Shearer, P. M. (2015). T phase observations in global seismogram stacks. *Geophysical Research Letters*, *42*(16), 6607-6613.

Callies, J., Wu, W., Peng, S., & Zhan, Z. (2023). Vertical-Slice Ocean Tomography With Seismic Waves. *Geophysical Research Letters*, *50*(8), e2023GL102881.

Candès, E., & Donoho, D. L. (2004). New tight frames of curvelets and optimal representations of objects with piecewise C2 singularities. *Communications on Pure and Applied Mathematics: A Journal Issued by the Courant Institute of Mathematical Sciences*, *57*(2), 219-266.

Candès, E., Demanet, L., Donoho, D., & Ying, L. (2006). Fast discrete curvelet transforms. *multiscale modeling & simulation*, *5*(3), 861-899.

Cheng, F., Chi, B., Lindsey, N. J., Dawe, T. C., & Ajo-Franklin, J. B. (2021). Utilizing distributed acoustic sensing and ocean bottom fiber optic cables for submarine structural characterization. *Scientific reports*, *11*(1), 1-14

Collins, M.P. (1936). *Bulletin Number 5*. Harvard University Seismograph Station, 23.

Das, R., Wason, H. R., & Sharma, M. L. (2011). Global regression relations for conversion of surface wave and body wave magnitudes to moment magnitude. *Natural hazards*, *59*, 801-810.

de Groot-Hedlin, C. D. (2005). Estimation of the rupture length and velocity of the Great Sumatra earthquake of Dec 26, 2004 using hydroacoustic signals. *Geophysical Research Letters*, *32*(11).

de Groot-Hedlin, C. D., & Orcutt, J. A. (2001). Excitation of T-phases by seafloor scattering. *The Journal of the Acoustical Society of America*, *109*(5), 1944-1954.

Dziak, R. P., Bohnenstiehl, D. R., Matsumoto, H., Fox, C. G., Smith, D. K., Tolstoy, M., ... & Fowler, M. J. (2004). P-and T-wave detection thresholds, Pn velocity estimate, and detection of lower mantle and core P-waves on ocean sound-channel hydrophones at the Mid-Atlantic Ridge. *Bulletin of the Seismological Society of America*, *94*(2), 665-677.

Dziak, R. P., Bohnenstiehl, D. R., & Smith, D. K. (2012). Hydroacoustic monitoring of oceanic spreading centers: Past, present, and future. *Oceanography*, *25*(1), 116-127.

Fang, J., Yang, Y., Shen, Z., Biondi, E., Wang, X., Williams, E. F., ... & Zhan, Z. (2023). Directional Sensitivity of DAS and Its Effect on Rayleigh-Wave Tomography: A Case Study in Oxnard, California. Seismological Society of America, 94(2A), 887-897.

Forget, G. A. E. L., Campin, J. M., Heimbach, P., Hill, C. N., Ponte, R. M., & Wunsch, C. (2015). ECCO version 4: An integrated framework for non-linear inverse modeling and global ocean state estimation. *Geoscientific Model Development*, *8*(10), 3071-3104.

Fox, C. G., Dziak, R. P., Matsumoto, H., & Schreiner, A. E. (1993). Potential for monitoring low-level seismicity on the Juan-de-Fuca ridge using military hydrophone arrays. Marine Technology Society Journal, 27(4), 22-30.

Fox, C. G., Radford, W. E., Dziak, R. P., Lau, T. K., Matsumoto, H., & Schreiner, A. E. (1995). Acoustic detection of a seafloor spreading episode on the Juan de Fuca Ridge using military hydrophone arrays. *Geophysical Research Letters*, *22*(2), 131-134.

Fox, C. G., Matsumoto, H., & Lau, T. K. A. (2001). Monitoring Pacific Ocean seismicity from an autonomous hydrophone array. *Journal of Geophysical Research: Solid Earth*, *106*(B3), 4183-4206.

Gutenberg, B., & Richter, C. F. (1944). Frequency of earthquakes in California. *Bulletin of the Seismological society of America*, *34*(4), 185-188.

Hamada, N. (1985). T waves recorded by ocean bottom seismographs off the south coast of Tokai area, central Honshu, Japan. *Journal of Physics of the Earth*, *33*(5), 391-410.

Hanson, J. A., & Bowman, J. R. (2006). Methods for monitoring hydroacoustic events using direct and reflected T waves in the Indian Ocean. *Journal of Geophysical Research: Solid Earth*, *111*(B2)

Hartog, A. H. (2017). *An introduction to distributed optical fibre sensors*. CRC press.

Hennenfent, G., & Herrmann, F. J. (2006). Seismic denoising with nonuniformly sampled curvelets. *Computing in Science & Engineering*, *8*(3), 16-25.

Hersbach, H., Bell, B., Berrisford, P., Biavati, G., Horányi, A., Munoz Sabater, J., ... & Thépaut, J. N. (2023). ERA5 hourly data on single levels from 1940 to present. *Copernicus Climate Change Service (C3S) Climate Data Store (CDS)*. 10.24381/cds.adbb2d47 (Accessed on 08-Aug-2023)

Hilmo, R., & Wilcock, W. S. (2020). Physical sources of high-frequency seismic noise on Cascadia Initiative ocean bottom seismometers. *Geochemistry, Geophysics, Geosystems*, *21*(10), e2020GC009085.

Hooft, E. E., Patel, H., Wilcock, W., Becker, K., Butterfield, D., Davis, E., ... & Stakes, D. (2010). A seismic swarm and regional hydrothermal and hydrologic perturbations: The northern Endeavour segment, February 2005. *Geochemistry, Geophysics, Geosystems*, *11*(12).

Hyndman, R. D., Riddihough, R. P., & Herzer, R. (1979). The Nootka fault zone—A new plate boundary off western Canada. *Geophysical Journal International*, *58*(3), 667-683.

Ide, S., Araki, E., & Matsumoto, H. (2021). Very broadband strain-rate measurements along a submarine fiber-optic cable off Cape Muroto, Nankai subduction zone, Japan. *Earth, Planets and Space*, *73*(1), 1-10

Jaggar, T. A. (1930). How the seismograph works. *The Volcano Letter*, *268*, 1–4.

Janiszewski, H. A., Eilon, Z., Russell, J. B., Brunsvik, B., Gaherty, J. B., Mosher, S. G., ... & Coats, S. (2023). Broad-band ocean bottom seismometer noise properties. *Geophysical Journal International*, *233*(1), 297-315.

Kelley, D. S., Delaney, J. R., & Juniper, S. K. (2014). Establishing a new era of submarine volcanic observatories: Cabling Axial Seamount and the Endeavour Segment of the Juan de Fuca Ridge. *Marine Geology*, *352*, 426-450.

Kennett, B. L. N., & Engdahl, E. R. (1991). Traveltimes for global earthquake location and phase identification. Geophysical Journal International, 105(2), 429-465.

Komatitsch, D., & Tromp, J. (1999). Introduction to the spectral element method for three-dimensional seismic wave propagation. *Geophysical journal international*, *139*(3), 806-822.Koyanagi, S., Aki, K., Biswas, N., & Mayeda, K. (1995). Inferred attenuation from site effect-corrected T phases recorded on the island of Hawaii. *Pure and Applied Geophysics*, *144*(1), 1-17.

Kuna, V. M., Nábělek, J. L., & Braunmiller, J. (2019). Mode of slip and crust–mantle interaction at oceanic transform faults. *Nature Geoscience*, *12*(2), 138-142.

Li, Z., Shen, Z., Yang, Y., Williams, E., Wang, X., & Zhan, Z. (2021). Rapid response to the 2019 Ridgecrest earthquake with distributed acoustic sensing. *AGU Advances*, *2*(2), e2021AV000395.

Lindsey, N. J., Dawe, T. C., & Ajo-Franklin, J. B. (2019). Illuminating seafloor faults and ocean dynamics with dark fiber distributed acoustic sensing. *Science*, *366*(6469), 1103-1107.

Lindsey, N. J., & Martin, E. R. (2021). Fiber-optic seismology. *Annual Review of Earth and Planetary Sciences*, *49*, 309-336.

Linehan, D. (1940). Earthquakes in the West Indian region. *Eos, Transactions American Geophysical Union*, *21*(2), 229-232.

Lior, I., Sladen, A., Rivet, D., Ampuero, J. P., Hello, Y., Becerril, C., ... & Markou, C. (2021). On the detection capabilities of underwater distributed acoustic sensing. *Journal of Geophysical Research: Solid Earth*, *126*(3), e2020JB020925.

Madariaga, R. (1976). Dynamics of an expanding circular fault. *Bulletin of the Seismological Society of America*, *66*(3), 639-666.

Martin, E. R., Lindsey, N. J., Ajo-Franklin, J. B., & Biondi, B. L. (2021). Introduction to interferometry of fiber-optic strain measurements. *Distributed Acoustic Sensing in Geophysics: Methods and Applications*, 111-129.

Matsumoto, H., Araki, E., Kimura, T., Fujie, G., Shiraishi, K., Tonegawa, T., ... & Karrenbach, M. (2021). Detection of hydroacoustic signals on a fiber-optic submarine cable. *Scientific reports*, *11*(1), 1-12.

Matsumoto, H., Haralabus, G., Zampolli, M., & Özel, N. M. (2016). T-phase and tsunami pressure waveforms recorded by near-source IMS water-column hydrophone triplets during the 2015 Chile earthquake. *Geophysical Research Letters*, *43*(24), 12-511.

McDougall, T. J., & Barker, P. M. (2011). Getting started with TEOS-10 and the Gibbs Seawater (GSW) oceanographic toolbox. *Scor/Iapso WG*, *127*(532), 1-28.

Muir, J. B., & Zhan, Z. (2021). Seismic wavefield reconstruction using a pre-conditioned wavelet–curvelet compressive sensing approach. *Geophysical Journal International*, *227*(1), 303-315.

Munk, W. H., Spindel, R. C., Baggeroer, A., & Birdsall, T. G. (1994). The heard island feasibility test. *The Journal of the Acoustical Society of America*, *96*(4), 2330-2342

Munk, W., & Wunsch, C. (1979). Ocean acoustic tomography: A scheme for large scale monitoring. *Deep Sea Research Part A. Oceanographic Research Papers*, *26*(2), 123-161

Okal, E. A. (2001). "Detached" deep earthquakes: are they really? *Physics of the Earth and Planetary Interiors*, *127*(1-4), 109-143.

Okal, E. A. (2008). The generation of T waves by earthquakes. *Advances in Geophysics*, *49*, 1-6

Okal, E. A., & Talandier, J. (1986). T-wave duration, magnitudes and seismic moment of an earthquake-application to tsunami warning. *Journal of Physics of the Earth*, *34*(1), 19-42.

Parnell-Turner, R., Smith, D. K., & Dziak, R. P. (2022). Hydroacoustic monitoring of seafloor spreading and transform faulting in the equatorial Atlantic Ocean. *Journal of Geophysical Research: Solid Earth*, *127*(7), e2022JB024008.

Riser, S. C., Freeland, H. J., Roemmich, D., Wijffels, S., Troisi, A., Belbéoch, M., ... & Jayne, S. R. (2016). Fifteen years of ocean observations with the global Argo array. *Nature Climate Change*, *6*(2), 145-153

Savard, G., Bostock, M. G., Hutchinson, J., Kao, H., Christensen, N. I., & Peacock, S. M. (2020). The northern terminus of Cascadia subduction. *Journal of Geophysical Research: Solid Earth*, *125*(6), e2019JB018453.

Simon, J. D., Simons, F. J., & Irving, J. C. (2021). A MERMAID miscellany: Seismoacoustic signals beyond the P wave. *Seismological Society of America*, *92*(6), 3657-3667.

Smith, D. K., Tolstoy, M., Fox, C. G., Bohnenstiehl, D. R., Matsumoto, H., & J. Fowler, M. (2002). Hydroacoustic monitoring of seismicity at the slow-spreading Mid-Atlantic Ridge. *Geophysical Research Letters*, *29*(11), 13-1.

Sladen, A., Rivet, D., Ampuero, J. P., De Barros, L., Hello, Y., Calbris, G., & Lamare, P. (2019). Distributed sensing of earthquakes and ocean-solid Earth interactions on seafloor telecom cables. *Nature communications*, *10*(1), 1-8

Spica, Z. J., Nishida, K., Akuhara, T., Pétrélis, F., Shinohara, M., & Yamada, T. (2020). Marine sediment characterized by ocean-bottom fiber-optic seismology. *Geophysical Research Letters*, *47*(16), e2020GL088360.

Talandier, J., & Okal, E. A. (2001). Identification criteria for sources of T waves recorded in French Polynesia. In *Monitoring the Comprehensive Nuclear-Test-Ban Treaty: Hydroacoustics* (pp. 567-603). Birkhäuser, Basel.

Talandier, J., Hyvernaud, O., Reymond, D., & Okal, E. A. (2006). Hydroacoustic signals generated by parked and drifting icebergs in the Southern Indian and Pacific Oceans. *Geophysical Journal International*, *165*(3), 817-834.

Talandier, J., & Okal, E. A. (2016). A new source discriminant based on frequency dispersion for hydroacoustic phases recorded by T-phase stations. *Geophysical Journal International*, *206*(3), 1784-1794.

Tepp, G., & Dziak, R. P. (2021). The seismo-acoustics of submarine volcanic eruptions. *Journal of Geophysical Research: Solid Earth*, 126(4), e2020JB020912.

Tolstoy, I., & Ewing, M. (1950). The T phase of shallow-focus earthquakes. *Bulletin of the Seismological Society of America*, *40*(1), 25-51.

Tréhu, A. M., Wilcock, W. S., Hilmo, R., Bodin, P., Connolly, J., Roland, E. C., & Braunmiller, J. (2018). The role of the Ocean Observatories Initiative in monitoring the offshore earthquake activity of the Cascadia subduction zone. Oceanography, 31(1), 104-113.

Uchida, N., & Bürgmann, R. (2019). Repeating earthquakes. *Annual Review of Earth and Planetary Sciences*, *47*(1), 305-332.

Ugalde, A., Becerril, C., Villaseñor, A., Ranero, C. R., Fernández-Ruiz, M. R., Martin-Lopez, S., ... & Martins, H. F. (2022). Noise Levels and Signals Observed on Submarine Fibers in the Canary Islands Using DAS. *Seismological Society of America*, *93*(1), 351-363

Viens, L., Bonilla, L. F., Spica, Z. J., Nishida, K., Yamada, T., & Shinohara, M. (2022). Nonlinear earthquake response of marine sediments with distributed acoustic sensing. *Geophysical Research Letters*, *49*(21), e2022GL100122.

Walker, D. A., McCreery, C. S., & Hiyoshi, Y. (1992). T-phase spectra, seismic moments, and tsunamigenesis. *Bulletin of the Seismological Society of America*, *82*(3), 1275-1305.

Webb, S. C. (1998). Broadband seismology and noise under the ocean. *Reviews of Geophysics*, *36*(1), 105-142.

Withers, M., Aster, R., Young, C., Beiriger, J., Harris, M., Moore, S., & Trujillo, J. (1998). A comparison of select trigger algorithms for automated global seismic phase and event detection. *Bulletin of the Seismological Society of America*, *88*(1), 95-106.

Wilcock, W. S., Abadi, S., & Lipovsky, B. P. (2023). Distributed acoustic sensing recordings of low-frequency whale calls and ship noise offshore Central Oregon. *JASA Express Letters*, *3*(2), 026002.

Williams, E. F., Fernández-Ruiz, M. R., Magalhaes, R., Vanthillo, R., Zhan, Z., González-Herráez, M., & Martins, H. F. (2019). Distributed sensing of microseisms and teleseisms with submarine dark fibers. *Nature communications*, *10*(1), 1-11.

Williams, E. F., Fernández-Ruiz, M. R., Magalhaes, R., Vanthillo, R., Zhan, Z., González-Herráez, M., & Martins, H. F. (2021). Scholte wave inversion and passive source imaging with ocean-bottom DAS. *The Leading Edge*, *40*(8), 576-583.

Williams, E. F., Zhan, Z., Martins, H. F., Fernandez-Ruiz, M. R., Martin-Lopez, S., Gonzalez-Herraez, M., & Callies, J. (2022). Surface gravity wave interferometry and ocean current monitoring with ocean-bottom DAS. *Journal of Geophysical Research: Oceans*, e2021JC018375

Wunsch, C. (2016). Global ocean integrals and means, with trend implications. *Annual Review of Marine Science*, *8*, 1-33.

Wech, A., Tepp, G., Lyons, J., & Haney, M. (2018). Using earthquakes, T waves, and infrasound to investigate the eruption of Bogoslof volcano, Alaska. *Geophysical Research Letters*, *45*(14), 6918-6925.

Wu, W., Zhan, Z., Peng, S., Ni, S., & Callies, J. (2020). Seismic ocean thermometry. *Science*, *369*(6510), 1510-1515.

Yu, C., Day, E. A., de Hoop, M. V., Campillo, M., & van der Hilst, R. D. (2017). Mapping mantle transition zone discontinuities beneath the Central Pacific with array processing of SS precursors. *Journal of Geophysical Research: Solid Earth*, *122*(12), 10-364.

Zhan, Z. (2020). Distributed acoustic sensing turns fiber-optic cables into sensitive seismic antennas. *Seismological Research Letters*, *91*(1), 1-15.

Zhang, J., & Langston, C. A. (2020). Separating the scattered wavefield from teleseismic P using curvelets on the long beach array data set. *Geophysical Journal International*, *220*(2), 1112-1127.

Zhou, Y., Chen, X., Ni, S., Qian, Y., Zhang, Y., Yu, C., ... & Xu, M. (2021). Determining crustal attenuation with seismic T waves in southern Africa. *Geophysical Research Letters*, *48*(15), e2021GL094410

*Journal of Geophysical Research: Solid Earth*

Supporting Information for

# Ocean bottom distributed acoustic sensing for *T*-wave detection and seismic ocean thermometry

Zhichao Shen[1] and Wenbo Wu[1]

[1]Department of Geology and Geophysics, Woods Hole Oceanographic Institution, Woods Hole, MA, USA

## Contents of this file

**Text S1. Earthquake origin time, location, and magnitude of NEPTUNE *T*-wave catalog**

To determine the origin times and locations of earthquakes in the NEPTUNE *T*-wave catalog, we perform a grid search by minimizing the misfit function $\psi = \sum_{i=1}^{n} \left| t_i^{predict} + t^{origin} - t_i^{pick} \right|$, where $n$ is the number of stations used for grid search. The origin time $t^{origin}$ is calculated as $t^{origin} = \frac{1}{n}\sum_{i=1}^{n}(t_i^{predict} - t_i^{pick})$, where $t_i^{predict}$ and $t_i^{pick}$ denote the predicted and picked seismic arrival time at *i*th station, respectively. We use a global 1D model IASP91 to calculate the predicted arrivals (Kennett & Engdahl, 1991). For *P*-waves and *S*-waves, we manually pick up their onset times on the vertical seismograms in a frequency band of 5-10 Hz. The searched area is bounded by 47°N and 52°N in latitude and 126°W and 132°W in longitude with an interval of 0.02°. When *P*-waves and *S*-waves are not available, event locations are constrained by *T*-waves. The arrival times of *T*-waves are picked at their envelop peaks and the searched grids are limited to seismic active areas (Figure S1a).

When clear *P*-waves and *S*-waves are available, we compute the local magnitude given as $M_L = logA + \log\left(\frac{D}{100}\right) + 0.00301 * (D - 100) + 3.0$ (Hutton & Boore, 1987), where A is the peak-to-peak amplitude of Wood Anderson type seismograms and *D* represents the epicentral distance. We convert the waveforms to Wood Anderson seismograph, filter them to 2-10 Hz, calculate the peak-to-peak amplitude and then compute the local magnitude by averaging over the three components of all available stations.

**Text S2. *T*-wave travel time sensitivity kernel**

We use the 2D spectral element method SPECFEM2D (Komatitsch & Tromp, 1999) to compute the *T*-wave travel time sensitivity kernels. Following Wu et al. (2023), we incorporate the global sediment and real bathymetry features to build a 3230 km (distance) X 40 km (depth) 2D slice model. A very shallow sea mountain present on the source-receiver great circle path seriously blocks the *T*-wave propagation, so we take another path, which corresponds to an effective source at 80 km further west, to avoid the strong blocking effects. The ocean sound speeds are calculated using the GSW package (McDougall & Barker, 2011) with the temperature and salinity inputs from the ECCOv4r4 climatology (Forget et al., 2015). The model is meshed with 20,000 (distance) X 96 (depth) elements to resolve 3.5 Hz *T*-wave. We cut the synthetic *T*-wave with a 60 s time window and run adjoint simulations to calculate the *T*-wave travel time sensitivity kernels (Figure S4).

**Text S3. *T*-wave amplitude ratio between NEPTUNE NCBC and OOI HYS11**

We download the east-component seismograms of the NEPTUNE station NCBC and the OOI station HYS11 for 27 ISC cataloged high-quality *T*-wave events around the Fox islands, bandpass filter the waveforms to 3-5 Hz, calculate the envelopes with a 5-s sliding smooth window, and compute the HYS11/NCBC peak amplitude ratios within a 150-s window after the predicted *T*-wave arrival times (Figure S5). The ISC body wave magnitude mb is converted to moment magnitude Mw using the empirical equation $M_w = (m_b^{ISC} - 1.65)/0.65$ (Das et al., 2011).

The HYS11/NCBC amplitude ratios have a mean number of 0.35 with a standard deviation of 0.07 (Figure S5). The consistent ratios indicate that *T*-waves at HYS11 and NCBC from earthquakes near the Fox islands share similar propagation effects, that allows us to use NCBC as a reference to synthesize *T*-wave at HYS11 from the Mw5.2 Fox island earthquake. The procedure works as follows: we download the HYS11 east-component seismograms of seven Mw5.3-5.9 earthquakes in this region (Figure S6); For each event, the corresponding *T*-wave is calibrated to Mw5.2 by scaling its own peak amplitude to $A_{HYS11}^{Mw5.2} = A_{NCBC}^{Mw5.2} * 0.35$, where $A_{NCBC}^{Mw5.2}$ is the observed NCBC *T*-wave peak amplitude from the Mw5.2 Fox Island event; Once the Mw5.2 *T*-waves at HYS11 are available, we can follow the same approach as that for the OOI North but use the seven Mw5.2 *T*-waves to conduct the SOT robustness analysis for HYS11 .

**Text S4. Correlation between the variations of OBDAS noise level and ocean dynamics**

We download wind significant wave height, wind speed, and wind direction data for the OOI OBDAS region from Copernicus Climate Change Service (C3S) Climate Data Store (CDS; DOI:10.24381/cds.adbb2d47). These parameters are commonly used to characterize the ocean swells and locally generated surface gravity waves. Notably, we observed substantial shifts in the ocean state over the course of the 4-day experiment (Figure S7). In particular, a sudden change in wind direction and significant wave height was recorded on November 4th, 2021, coinciding with the initiation of the increase in OBDAS noise level on the same date.

**Text S5. Influence of OBDAS noise level on its performance for SOT**

We randomly select 20 noise samples from the first 24 hours and another 20 noise samples for the last 24 hours, representing low and high noise levels, respectively. We generate 190 pseudo-repeating pairs for each testing earthquake magnitude in each noise level scenario and compute the corresponding SOT robustness and cross-correlation amplitude peaks. It is clear that the high noise level results in deterioration in SOT performance (Figure S8).

**Text S6. Testing different noise percentile thresholds for the stochastic removal**

Following the method used in Figure 11a, we randomly select 20 noise windows and generate 190 pseudo-repeating OBDAS pairs for different earthquake magnitudes ranging from M2.7 to M4.1. For each magnitude, we test six different noise thresholds from 50$^{th}$ percentile to 100$^{th}$ percentile of selected noise for the stochastic removal. After the curvelet denoising, we conduct the SOT measuring for each repeating pair and examine the time shift retrieval. Overall, using the six noise thresholds yields comparable SOT performance, in terms of SOT robustness, across the tested earthquake magnitude range (Figure S9).

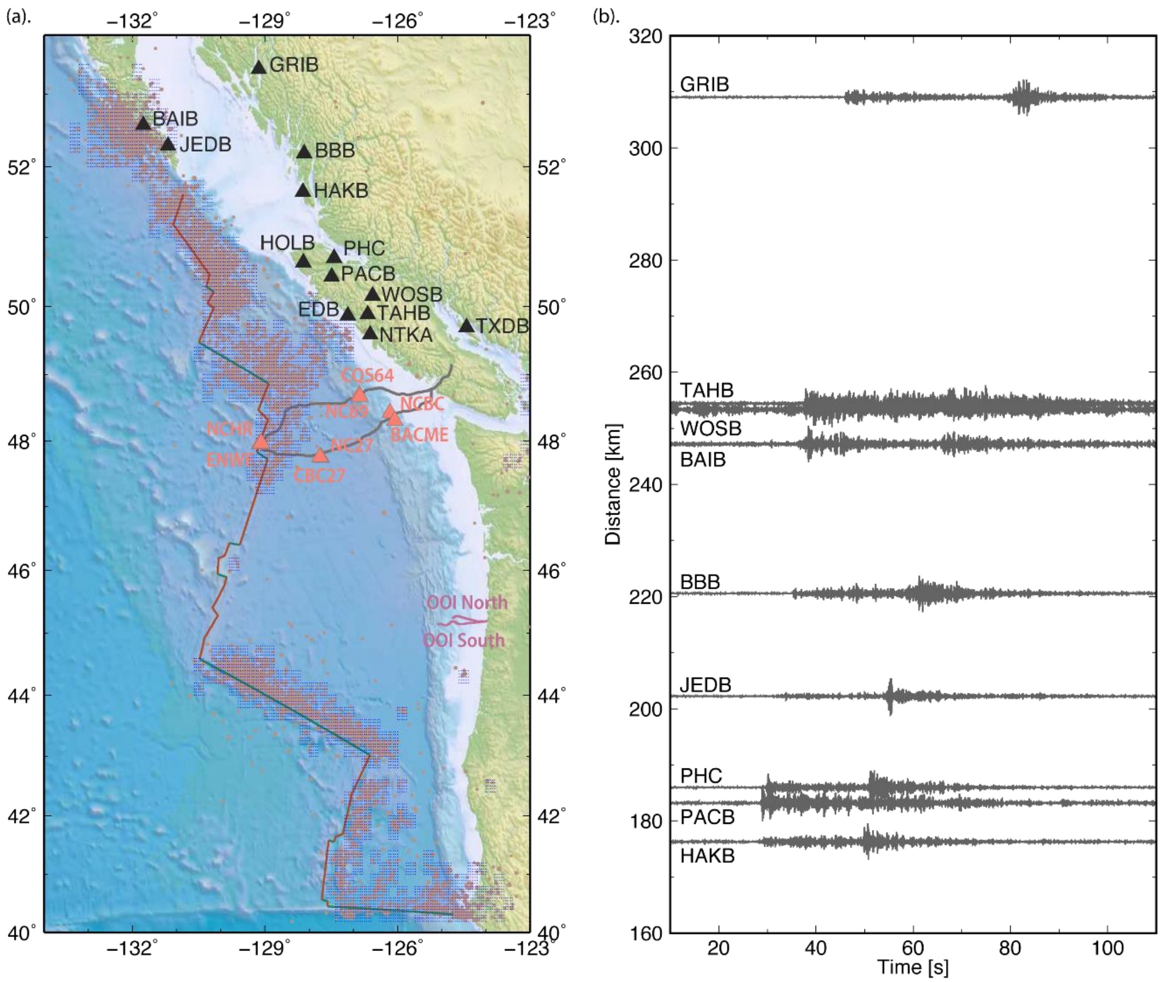


**Figure S1.** (a). Map of background seismicity (dark gray circles), grid-search locations (blue dots) and seismic stations used for locating earthquakes. Black triangles are land stations of which clear *P*-waves and *S*-waves are observed and used for locating earthquakes. (b). An example of *P*-waves and *S*-waves (5-10 Hz) recorded at onshore stations from Event No.11 in Table S1.

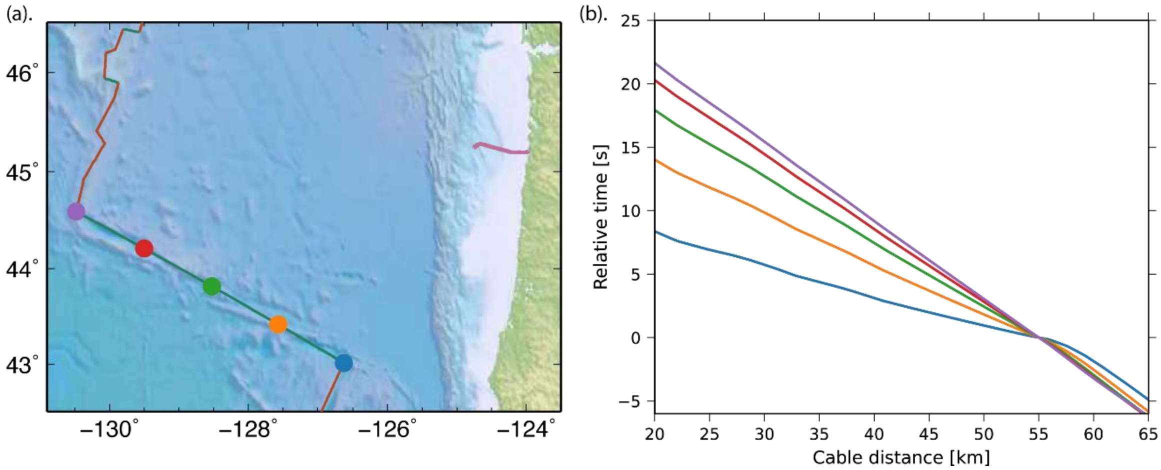


**Figure S2.** OOI North *T*-wave slowness sensitivity to earthquake location. (a). Map view of five equally spaced Blanco earthquake testing locations and the OOI North OBDAS. (b). Theoretical *T*-wave arrival times on OOI North, relative to that at a cable distance of 55km. Each line shows the arrival times of corresponding testing location in (a). Note the arrival time kinks around 55 km due to a cable geometry change.

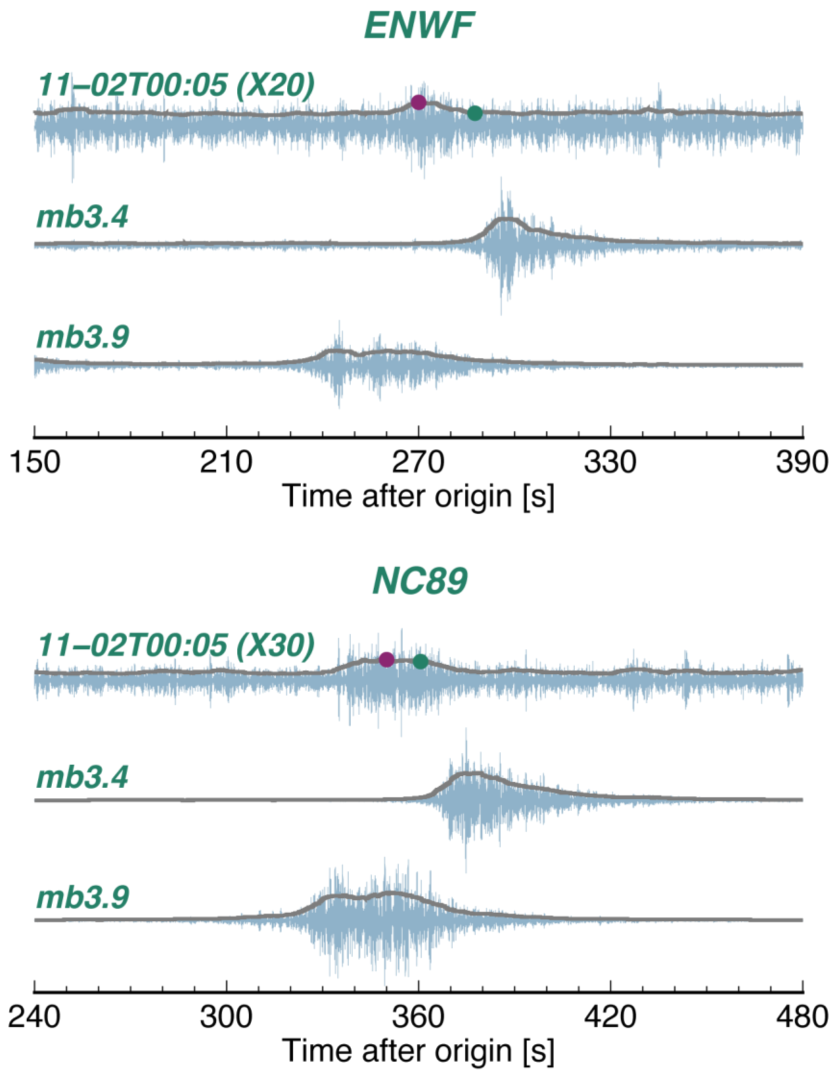


**Figure S3.** *T*-waves observed at two NEPTUNE stations from the 11-02T00:05 Blanco earthquake and two Blanco events (mb3.9 & mb3.4) occurred in 2021-11-01 as shown in Figure 13. The waveforms are bandpass filtered between 4-8 Hz, the gray lines and green dots represent the corresponding envelopes and predicted *T*-wave arrival times from the estimated location of the 11-20T00:05 event in Figure 9, respectively. It is hard to identify *T*-waves at other NEPTUNE stations due to their high noise levels.

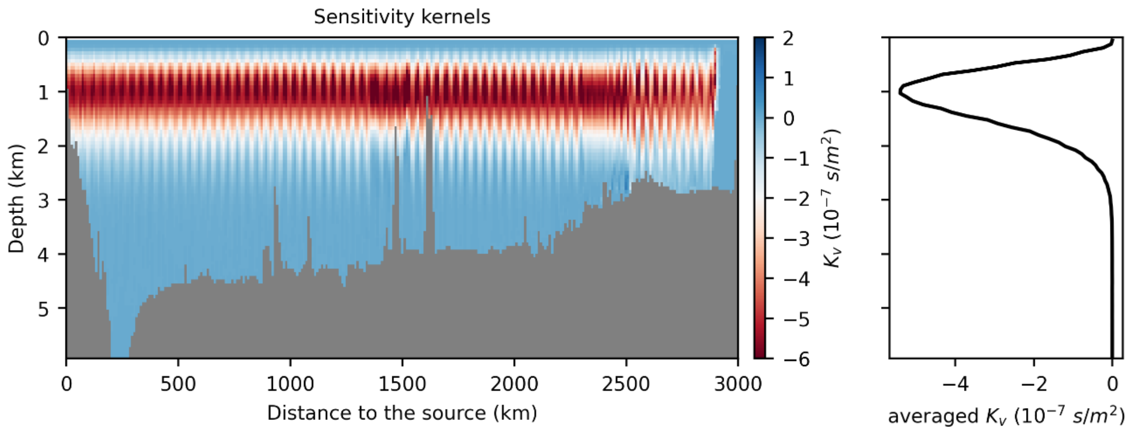


**Figure S4.** *T*-wave travel time sensitivity kernel (2.5-3.5 Hz) for the Aleutian-OOI path. The right panel is the averaged *T*-wave sensitivity kernel along the path.

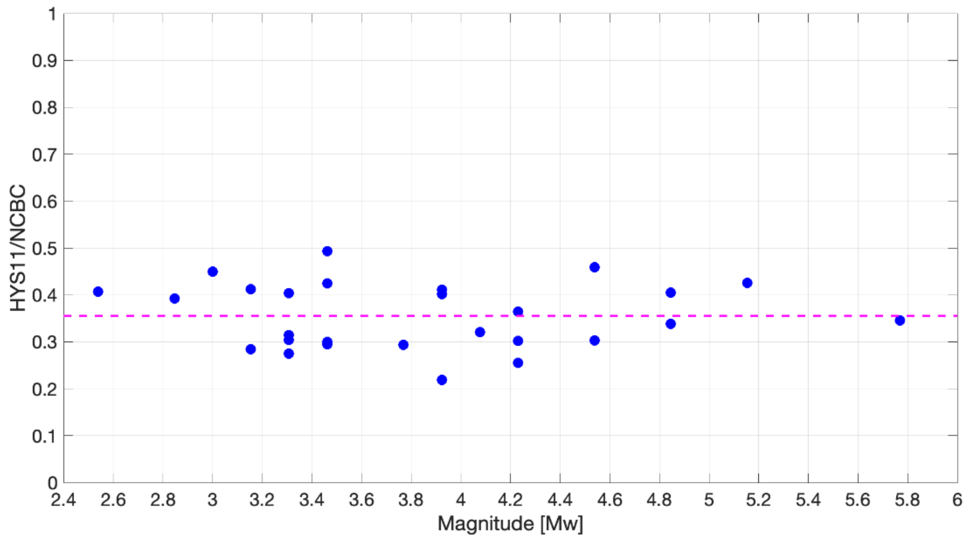


**Figure S5.** Amplitude ratios of *T*-wave envelopes between OOI HYS11 and NEPTUNE NCBC for ISC catalogued earthquakes near the Fox Islands. The dashed line is the averaged ratio (~0.35) among all the data points.

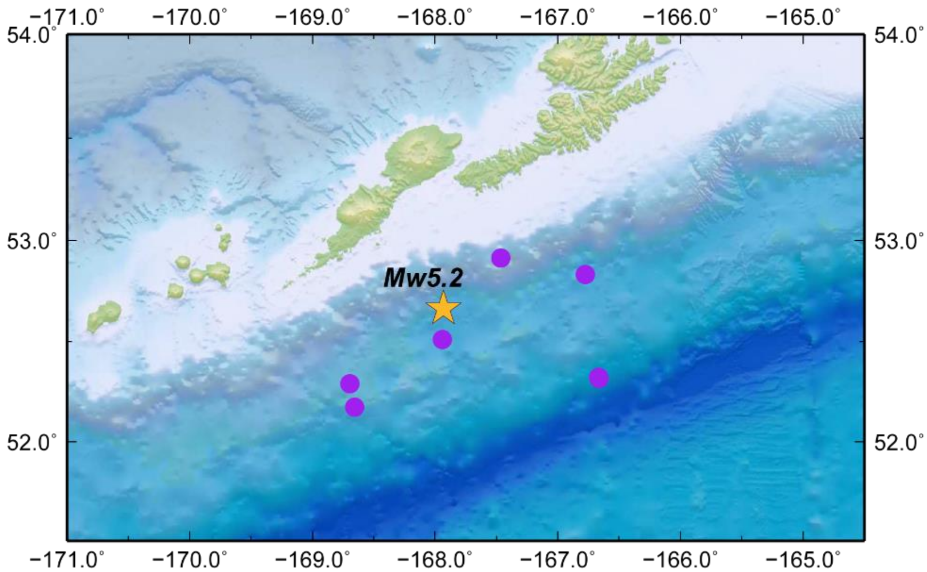


**Figure S6.** Seven moderate size events (purple circles) used in calculating the SOT robustness of HYS11. It is noted that the locations of two events overlap, making them visually hard to distinguish.

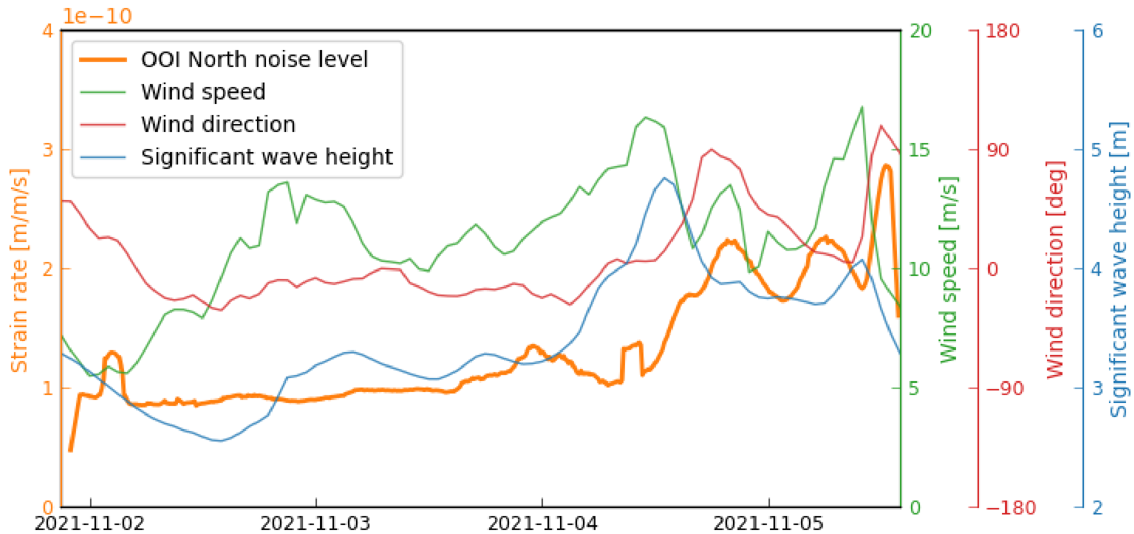


**Figure S7**. Comparison of OBDAS noise level, wind speed (at 10 m above the sea surface), wind direction and significant wave height.

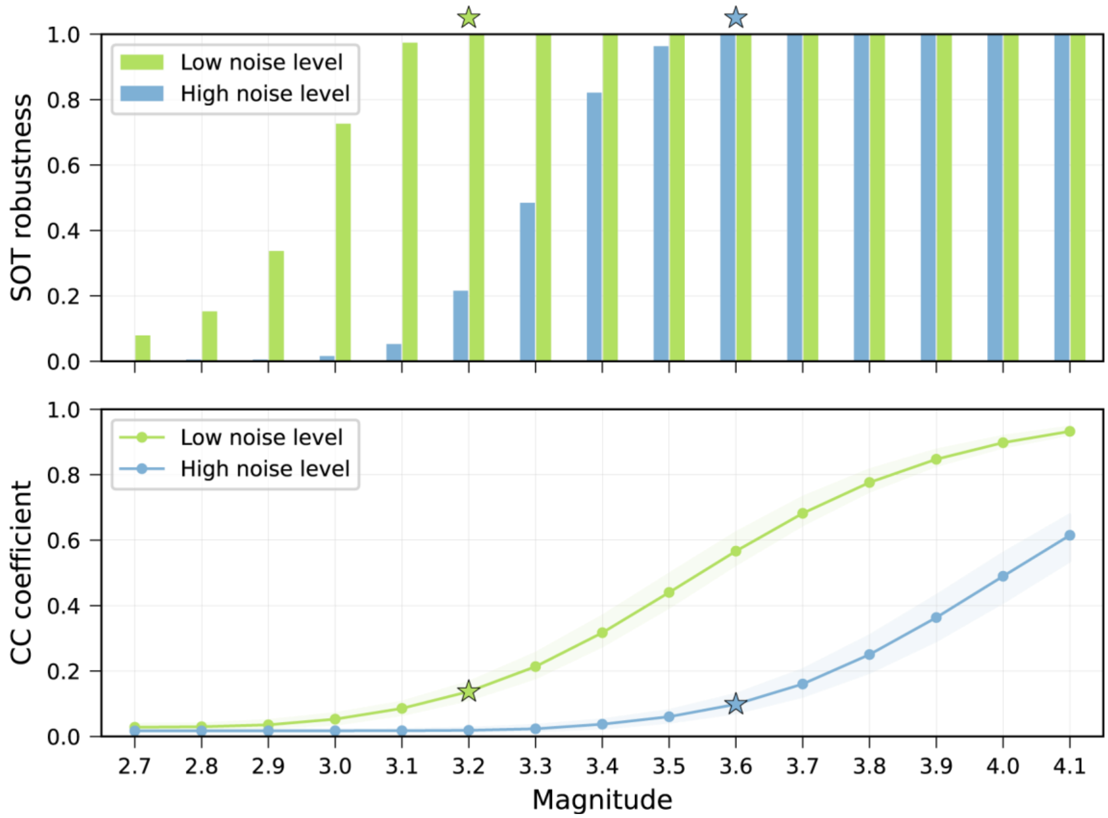


**Figure S8.** Noise effect on OBDAS performance for SOT. (a). Comparison of SOT robustness between low noise level scenario and high noise level scenario for denoised OOI North OBDAS data. (b). Corresponding cross-correlation amplitude between low noise level and high noise level on OBDAS. The stars mark the minimum magnitudes that yield reliable time shift measurements.

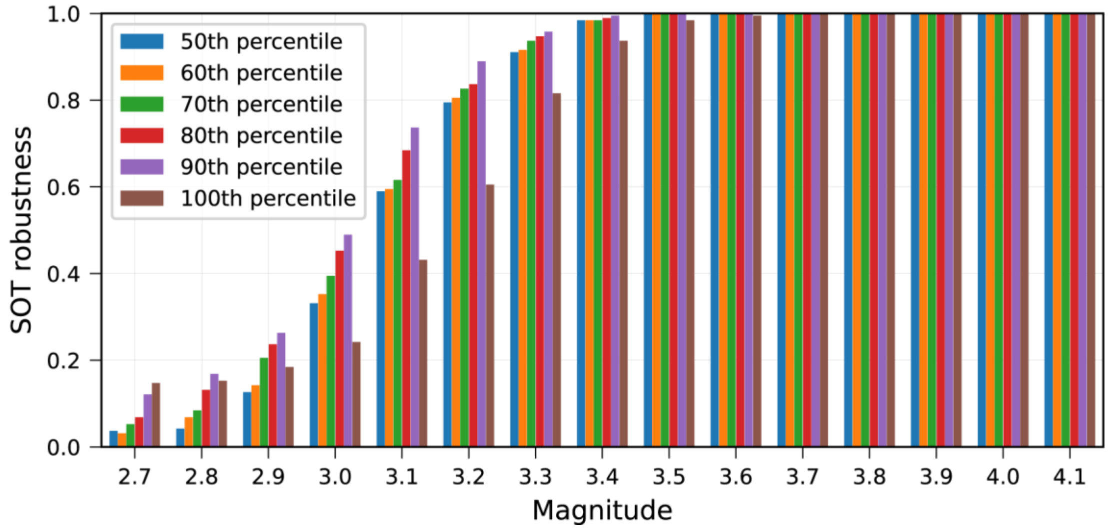


**Figure S9.** Effects of noise threshold in stochastic removal on the OBDAS performance for SOT.

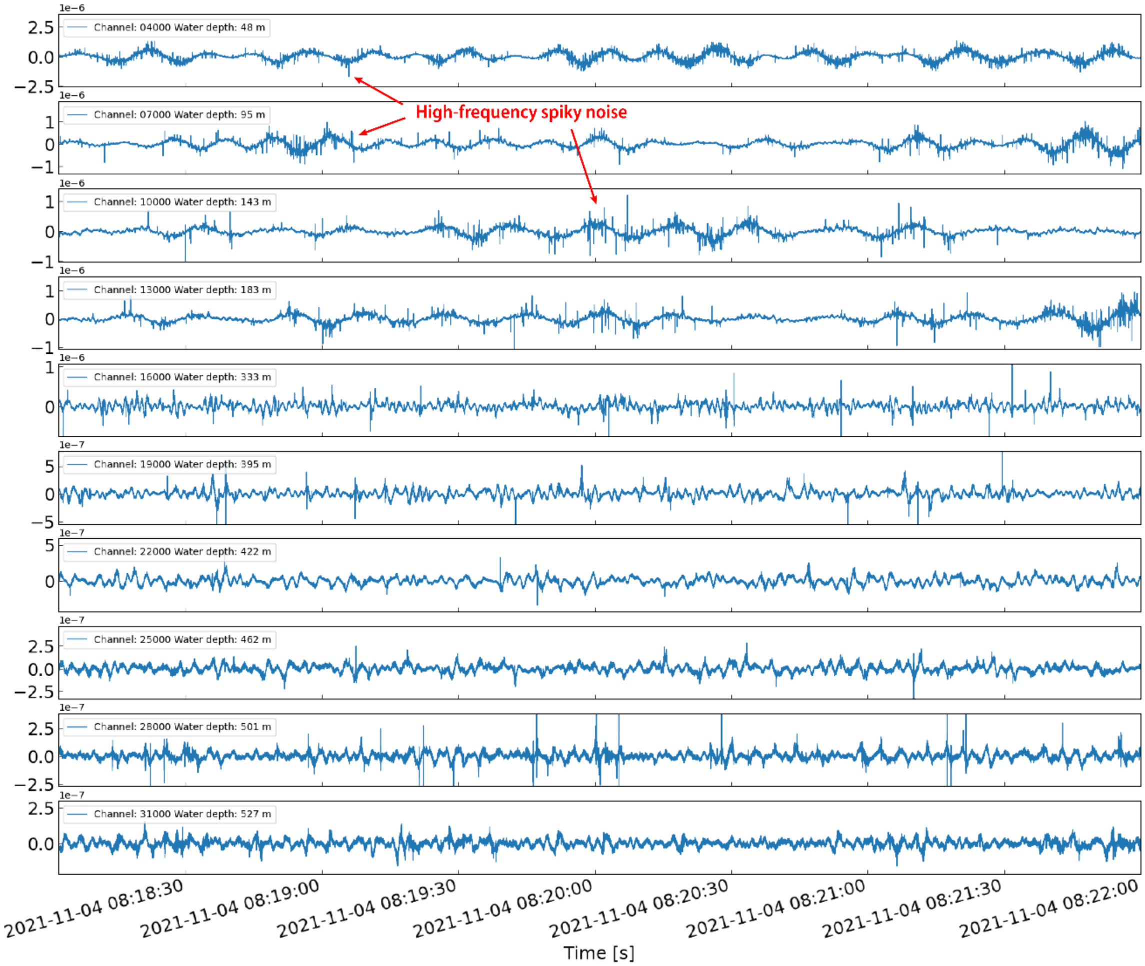


**Figure S10.** 4-min raw strain rate waveforms recorded at OOI North. The channel index is indicated at the top left. Strong high-frequency noises emerge at the peaks and troughs of ocean gravity waves. These noises become weaker in channels at larger ocean depths. Note that the y-axis has a different scale in each subplot.

| No. | Event time (UTC) | Latitude | Longitude | Depth [km] | Magnitude | Data used for location |
|---|---|---|---|---|---|---|
| 1 | 2021-11-01 22:59:13.64 | 47.20° | -129.20° | 10.0* | -- | *T*-wave |
| 2 | 2021-11-01 23:19:59.70 | 49.16° | -128.32° | 10.0* | ML1.6 | *P*-, *S*-waves |
| **3** | **2021-11-02 00:11:12.64** | **43.90°** | **-129.55°** | **10.0*** | **--** | ***T*-wave** |
| **4** | **2021-11-02 02:14:38.88** | **50.24°** | **-129.82°** | **10.0*** | **ML2.3** | ***P*-, *S*-waves** |
| **5** | **2021-11-02 05:41:35.24** | **50.40°** | **-129.78°** | **10.0*** | **ML1.7** | ***P*-, *S*-waves** |
| **6** | **2021-11-02 08:47:56.82** | **47.85°** | **-128.90°** | **10.0*** | **--** | ***T*-wave** |
| **7** | **2021-11-02 12:02:44.29** | **43.35°** | **-127.10°** | **10.0*** | **--** | ***T*-wave** |
| 8 | 2021-11-02 13:13:46.84 | 47.75° | -128.60° | 10.0* | -- | *T*-wave |
| **9** | **2021-11-02 15:01:05.13** | **47.20°** | **-129.20°** | **10.0*** | **--** | ***T*-wave** |
| 10 | 2021-11-02 18:01:17.36 | 49.17° | -128.00° | 10.0* | MLSn2.0 | ISC catalog |
| **11** | **2021-11-02 18:15:17.79** | **50.49°** | **-130.16°** | **10.0*** | **MLSn2.5** | **ISC catalog** |
| 12 | 2021-11-03 00:24:50.73 | 40.35° | -124.28° | 27.5 | Mw4.4 | ISC catalog |
| 13 | 2021-11-03 03:33:51.87 | 49.08° | -128.06° | 10.0* | ML1.8 | *P*-, *S*-waves |
| **14** | **2021-11-03 15:43:07.68** | **47.80°** | **-129.40°** | **10.0*** | **--** | ***T*-wave** |
| **15** | **2021-11-03 16:20:18.26** | **47.75°** | **-128.90°** | **10.0*** | **--** | ***T*-wave** |
| 16 | 2021-11-04 01:59:52.31 | 47.45° | -128.65° | 10.0* | -- | *T*-wave |
| **17** | **2021-11-04 03:43:21.34** | **44.20°** | **-129.05°** | **10.0*** | **--** | ***T*-wave** |
| 18 | 2021-11-04 05:15:01.55 | 48.65° | -128.35° | 10.0* | -- | *T*-wave |
| **19** | **2021-11-04 05:48:50.15** | **44.40°** | **-129.20°** | **10.0*** | **--** | ***T*-wave** |
| **20** | **2021-11-04 08:57:06.93** | **52.67°** | **-167.93°** | **39.3** | **Mw5.2** | **ISC catalog** |

| | | | | | | |
|---|---|---|---|---|---|---|
| 21 | 2021-11-04 10:23:49.43 | 47.85° | -128.55° | 10.0* | -- | *T*-wave |
| **22** | **2021-11-04 14:38:35.49** | **44.70°** | **-129.05°** | **10.0*** | **--** | ***T*-wave** |
| **23** | **2021-11-04 19:17:15.98** | **54.73°** | **-156.92°** | **10.0** | **mb4.5** | **ISC catalog** |
| 24 | 2021-11-04 20:16:14.48 | 47.20° | -128.80° | 10.0* | -- | *T*-wave |
| **25** | **2021-11-04 20:32:16.45** | **43.60°** | **-128.90°** | **10.0*** | **--** | ***T*-wave** |
| **26** | **2021-11-04 23:39:17.62** | **54.69°** | **-156.91°** | **10.0** | **mb4.0** | **ISC catalog** |
| **27** | **2021-11-05 05:12:49.48** | **43.60°** | **-128.40°** | **10.0*** | **--** | ***T*-wave** |

**Table S1.** *T*-wave catalog during the OOI DAS experiment using the NEPTUNE array. Symbol * denotes that the depth is fixed at 10 km. Earthquakes highlighted in red bold font generate identified *T*-waves on OOI DAS.